

The Martian photoelectron boundary as seen by MAVEN

P. Garnier,¹M. Steckiewicz,¹C. Mazelle,¹S. Xu,^{2,3}D. Mitchell,²M.K.G. Holmberg,¹J. S. Halekas,⁴L. Andersson,⁵D. A. Brain,⁵J.E.P. Connerney,⁶J. R. Espley,⁶R. J. Lillis,²J. G. Luhmann,²J.-A. Sauvaud,¹B. M. Jakosky⁵

¹IRAP, Université de Toulouse, CNRS, UPS, CNES, Toulouse, France.

²Space Sciences Laboratory, University of California, Berkeley, USA.

³Department of Climate and Space Sciences and Engineering, University of Michigan, Ann Arbor, Michigan, USA.

⁶NASA Goddard Space Flight Center, Greenbelt, USA.

⁵Laboratory for Atmospheric and Space Physics, University of Colorado, Boulder, USA.

⁴Department of Physics and Astronomy, University of Iowa, Iowa City, Iowa, USA.

Key Points:

- We determined the influence of the main driving parameters on the altitude of the PhotoElectron Boundary (PEB)
- We identified clear plasma and magnetic field characteristics of the PEB, and discuss its nature with respect to the ionopause
- We show how the PEB dynamics modifies the tail cross section used for estimating the photoelectrons (and associated ions) escape rate

This is the author manuscript accepted for publication and has undergone full peer review but has not been through the copyediting, typesetting, pagination and proofreading process, which may lead to differences between this version and the [Version of Record](#). Please cite this article as doi: [10.1002/2017JA024497](https://doi.org/10.1002/2017JA024497)

Corresponding author: P. GARNIER, philippe.garnier@irap.omp.eu

Abstract

Photoelectron peaks in the 20-30 eV energy range are commonly observed in the planetary atmospheres, produced by the intense photoionization from solar 30.4 nm photons. At Mars, these photoelectrons are known to escape the planet down its tail, making them tracers for the atmospheric escape. Furthermore, their presence or absence allow to define the so-called PhotoElectron Boundary (PEB), that separates the photoelectron dominated ionosphere from the external environment. We provide here a detailed statistical analysis of the location and properties of the PEB based on the Mars Atmosphere and Volatile Evolution (MAVEN) electron and magnetic field data obtained from September 2014 until May 2016 (including 1696 PEB crossings).

The PEB appears as mostly sensitive to the solar wind dynamic and crustal fields pressures. Its variable altitude thus leads to a variable wake cross section for escape (up to $\sim +50\%$), which is important for deriving escape rates. The PEB is not always sharp, and is characterized on average by : a magnetic field topology typical for the end of Magnetic Pile Up Region above it, more field aligned fluxes above than below, and a clear change of the altitude slopes of both electron fluxes and total density (that appears different from the ionopause). The PEB thus appears as a transition region between two plasma and fields configurations determined by the draping topology of the interplanetary magnetic field around Mars and much influenced by the crustal field sources below, whose dynamics also impacts the estimated escape rate of ionospheric plasma.

Introduction

Due to the absence of a strong intrinsic magnetic field, the thin Martian atmosphere directly interacts with the incident solar wind plasma. The ionized part of the atmosphere acts as a conductive obstacle, leading to a draping of the interplanetary magnetic field (IMF) around the planet and the formation of an induced magnetosphere.

Among the numerous processes at work in the Martian environment, the continuous ionization of the atmospheric neutrals by the extreme ultraviolet (EUV) photons from the Sun leads to the production of photoelectrons that play a key role in the heating balance of the atmosphere. In particular, the strong 30.4 nm Helium-II line of the solar spectrum ionizes CO_2 and O atmospheric neutrals [Mantas and Hanson, 1979], that can be seen in

48 the energy spectra of electrons at Mars or other bodies such as Titan, Venus and Earth
49 [Coates *et al.*, 2011] as two peaks between 21 and 24 eV and at 27 eV.

50 The Mars Global Surveyor (MGS) MAG/ER instrument revealed a strong change of
51 the electron spectra at the external limit of the ionosphere (Mitchell *et al.* [2000] ; Mitchell
52 *et al.* [2001]), with in particular a photoelectron boundary (PEB) or ionopause defined
53 by the disappearing of photoelectron features in the 20 – 50 eV energy range as well as
54 near 500 eV (i.e. Auger electrons) and a change of the slope below 100 eV. These au-
55 thors already mentioned the possible influence of crustal fields on the altitude of the ob-
56 served boundary. The finer energy resolution ($\delta m/m = 7\%$ compared to 25% for MGS)
57 of the Mars Express ASPERA ELS instrument [Barabash *et al.*, 2006] then allowed the
58 two photoelectron peaks in the 20 – 30 eV range to be resolved and the plasma boundaries
59 at Mars to be investigated in more details [Lundin *et al.*, 2004]. Frahm *et al.* [2006] and
60 Frahm *et al.* [2010] also revealed that a portion of the photoelectrons actually escape down
61 to the tail behind the planet along draped open field lines, thus providing an insight into
62 the escape rate of ionospheric plasma assuming overall neutrality of the plasma (see also
63 Liemohn *et al.* [2006] who modeled the magnetic connectivity for martian photoelectrons
64 from the dayside to the wake). Such photoelectrons are known to be common in planetary
65 atmospheres, such as at Titan, Venus, or Earth (see Coates *et al.* [2011], Wellbrock *et al.*
66 [2012], Tsang *et al.* [2015]).

67 Nevertheless, the definition of the Martian plasma boundaries still raises debates re-
68 garding their nature depending on the parameters observed (composition, density gradient,
69 magnetic topology, pressure balance etc.). In particular, the PEB (determined from the
70 disappearance of CO₂ 20 – 30 eV photoelectrons) and the ionopause (determined from
71 electron density gradients or density levels) were often observed at the same locations, but
72 not systematically. Han *et al.* [2014] used Mars Express MARSIS and ASPERA data from
73 2005 to 2013 to obtain a median altitude of the ionopause at about 450 km, while the
74 PEB altitude was located 200 km above this. However, no detailed analysis of the bound-
75 ary characteristics or drivers of influence was performed, except for the solar zenith angle
76 (SZA) variability.

77 The Mars Atmosphere and Volatile Evolution (MAVEN) mission, designed to study
78 the structure, composition and variability of the upper atmosphere and ionosphere of Mars,
79 reached Mars in September 2014 [Jakosky *et al.*, 2015]. The complete plasma and mag-

netic field instruments package, combined with the spacecraft's elliptical orbits reaching low altitudes (down to 110 km during deep-dip campaigns) allows us to analyze the Martian plasma environment and the ionosphere in more detail. Recently, *Sakai et al.* [2015] used a two-stream electron transport code to interpret the photoelectron and Auger electron observations of the MAVEN Solar Wind Electron Analyzer (SWEA) instrument [Mitchell et al., 2016]. They showed in particular how the solar irradiance, external electron fluxes and ionospheric thermal electron density control the photoelectron spectrum. *Xu et al.* [2016a] also showed the presence of photoelectrons in the nightside ionosphere, very likely due to transport along closed crustal magnetic field loops that cross the terminator and extend far into the deep nightside.

In this paper, we use MAVEN electron and magnetic field data to analyze the photoelectron boundary in detail. After a description of the instruments and dataset used for the study (section 1), we will discuss the geographical distribution of the boundary crossings (section 2) and the parameters driving its variability (section 3). We will then discuss the influence of the PEB on photoelectron escape (section 4), before we characterize in details the boundary itself and its near environment through several parameters (section 5) and end with conclusions (section 6).

1 Description of the dataset

1.1 Description of the instruments

The MAVEN Solar Wind Electron Analyzer (SWEA) instrument is a symmetric, hemispheric electrostatic analyzer with deflectors [Mitchell et al., 2016]. It is designed to measure the energy and angular distributions of electrons within an energy range of 3 to 4600 eV, with an energy resolution of $\delta E/E = 17\%$ and maximum time resolution of 2 seconds (depending on the mode used). MAVEN is not a spinning spacecraft but a three-axis stabilized spacecraft, so that SWEA uses deflectors to sweep the field of view (of $360^\circ * 7^\circ$ for the hemispheres) to reach a maximum FOV of $360^\circ * 120^\circ$ (i.e. 87% of the sky).

Moreover, we will use in this study the magnetic field measurements provided by the MAG instrument. It consists of two independent tri-axial fluxgate magnetometer sensors, which measure the ambient vector magnetic field at an intrinsic sample rate of 32 vector samples per second over a wide dynamic range (until 65,536 nT per axis) with a

111 maximum resolution of $0.008 nT$ and an accuracy of better than 0.05% [Connerney *et al.*,
112 2015].

113 1.2 The photoelectron boundary dataset

114 Figure 1 shows an example of a peripasis passage of MAVEN in February 2015,
115 with the SWEA energy spectrograms and orbital parameters. The (X,Y,Z) coordinates are
116 given in the MSO frame, where X points towards the Sun, Y points approximately oppo-
117 site to Mars orbital angular velocity and Z completes the right-handed set. The spacecraft
118 was thus at first located in the dayside southern magnetosheath (a shocked and heated
119 spectrum typical for the magnetosheath at 02:12 is shown in panel e), with a draping and
120 strong gradient of the magnetic field (not shown) from 02:13 UT, until a large drop of the
121 energetic electron fluxes at about 02:18 UT and the appearance of the strong photoelec-
122 tron peak at 20 – 30 eV. The spacecraft thus enters the ionosphere (a typical spectrum
123 at 02:24 UT is shown in panel d) and reaches the terminator region near 02:30 UT. The
124 photoelectron double peak (between 21 and 24 and at 27 eV) appears as a single peak due
125 to the energy resolution of the instrument (except during negative charging events where
126 the line splits into two different lines). Please note that the broad energy peak around 60
127 eV seen in the magnetosheath spectrum at 02.12 is not associated with photoelectrons but
128 is a typical feature of the heated solar wind particles. A suprathermal electron depletion
129 is then observed around periapsis (02:36 UT to 02:42 UT), since the spacecraft is located
130 in the low altitude nightside ionosphere where the absorption by CO_2 neutrals depletes
131 almost all suprathermal electrons while the major ionization process - i.e. photoioniza-
132 tion - is stopped (see *Steckiewicz et al.* [2015] or *Steckiewicz et al.* [2017] for further de-
133 tails). The CO_2 photoelectron line at 20 – 30 eV thus disappears as the spacecraft moves
134 through the depletion region, and reappears at 02:42 UT where it appears again until the
135 end of the period shown, while the spacecraft is located behind the terminator in the tail :
136 these photoelectrons are thus escaping the planet, with a line more diffuse than in the deep
137 ionosphere (see also *Coates et al.* [2015] and *Tsang et al.* [2015] for similar observations at
138 Venus).

139 The three dashed lines in figure 1 show where the photoelectron line appears or dis-
140 appears during this case study, corresponding to either the PEB (near 02 : 19) or to the
141 edges of the electron depletions (at 02 : 35 and 02 : 42). We analyzed by hand the SWEA
142 spectrograms and energy spectra from September 2014 to end of May 2016, and identified

143 3022 timings where the photoelectron line appeared or disappeared. An automatic (peak)
144 detection algorithm was used at first, which worked well for large photoelectron peaks be-
145 low the PEB, but it could hardly detect precisely the faint peaks that often appear close to
146 the PEB (all the more that intermittent photoelectron line crossings are considered as PEB
147 crossings). More than half of the automatic crossings timings had to be corrected by a few
148 minutes, so that we chose to define the crossings manually for a better precision. The au-
149 tomatic algorithm will be however discussed in a future paper on a statistical analysis of
150 the ionospheric photoelectrons.

151 Among these 3022 crossings, 1696 correspond unambiguously to dayside PEB cross-
152 ings, the rest corresponding to : edges of electron depletions in the nightside (all suprath-
153 ermal electron fluxes drop, including the photoelectron fluxes), edges of detached escaping
154 photoelectrons in the wake, or ambiguous crossings below the extreme ultraviolet termina-
155 tor (here defined by a minimum altitude of 140 km). We thus defined as PEB crossings
156 only the photoelectron line crossings taking place on the dayside ($X > 0$) at altitudes
157 above the EUV terminator (see also later figure 3). The timings of the crossings are de-
158 fined with a precision of ~ 30 seconds, and define the last (or first) time interval where
159 the photoelectron peak at $20 - 30$ eV is unambiguously observed. The crossings on the
160 dayside are easier to determine, whereas the times where the photoelectron line appears or
161 disappears in the tail or nightside ionosphere are much more difficult to define precisely
162 due to the more diffuse structure of the peak. A number of small nightside electron deple-
163 tions are also not included in the total dataset, as well as temporary crossings in the tail
164 where the line is more intermittent, due to the strong plasma dynamics (mixing of sev-
165 eral populations, accelerated particles, etc.) occurring in this region. As will be discussed
166 later, the PEB, even on the dayside, can barely be defined with a high precision due to
167 the interpretation of the spectra which often show faint peaks before showing strong un-
168 ambiguous peaks. The PEB appears as a transition region where the photoelectron flux
169 gradually decreases, more or less sharp depending on the conditions (see section 5).

170 **2 Geographical distribution of the PEB**

171 **2.1 Overall distribution**

172 Figure 2 shows the geographical distribution of the 3022 photoelectron line cross-
173 ings (1696 PEB crossings) in MSO cylindrical coordinates. No crossing was found at

174 low SZA values (i.e. below 10° SZA) due to the orbital characteristics of MAVEN with
175 few passages at the appropriate altitudes below 10° SZA. The PEB crossings cover a SZA
176 range from $\sim 10^\circ$ SZA to $\sim 90^\circ$ SZA. Almost all crossings were confined within the aver-
177 age Magnetic Pile-Up Boundary fit by *Trotignon et al.* [2006] determined from the Phobos
178 2 and Mars Global Surveyor data sets, in a shell of about $0.15 - 0.2 R_M$ ($1R_M \approx 3390$ km
179 average Martian radius).

180 The altitude of the dayside PEB crossings strongly varies between 186 and 1931
181 km, with median and average altitudes respectively at 528 and 573 km (without including
182 any SZA dependency). This is in close agreement with the Mars Express results by *Han*
183 *et al.* [2014] who obtained an average altitude between 553 and 633 km depending on the
184 SZA regime. The suprathermal electrons, thanks to their large mean free path and cross
185 field diffusion in the absence of open draped lines, thus transport vertically to high alti-
186 tudes (compared to the suprathermal electron exobase at $\sim 145 - 165$ km, see *Xu et al.*
187 [2016b]), and are stopped on average before the other plasma boundaries such as the Ion
188 Composition Boundary (ICB), Magnetic-Pile-Up Boundary (MPB) or pressure β^* Bound-
189 ary (*Xu et al.* [2016c] ; *Matsunaga et al.* [2015]). We can mention that the MPB (named
190 like this by numerous authors, see initially *Nagy et al.* [2004] or *Bertucci et al.* [2004])
191 is also often called Induced Magnetosphere Boundary (cf. *Dubin et al.* [2006] or *Brain*
192 *et al.* [2017]), after it was even called at first planetopause [*Riedler et al.*, 1989] or magne-
193 topause [*Rosenbauer et al.*, 1989].

194 Except near noon (see below for further details), the southern median location (yel-
195 low line) of the PEB is always at higher altitudes than the northern one (cyan line), in
196 particular close to the terminator where the difference reaches ~ 200 km, presumably due
197 to the influence of the strong crustal magnetic fields of the southern hemisphere, which
198 will be further discussed in section 3. The thickness of the altitude shell (defined by e.g.
199 80% of the PEB crossings inside the shell, magenta lines) increases from about 230 km at
200 low SZA values until ~ 800 km near the terminator, as expected from the topology of the
201 draping of the IMF around the planet that is more variable at terminator than at noon (as
202 seen for the MPB location, see *Trotignon et al.* [2006]).

203 A conic fitting of the dayside PEB crossings - defined by $r = \frac{L}{1+e*\cos(\theta)}$ with r and
204 θ polar coordinates with origin at X_0 referenced to the X-axis, and L and e the semi-latus
205 rectum and eccentricity ; see *Edberg et al.* [2008] for further details - provides the fol-

206 lowing results : $(X_0, L, e) = (0 R_M, 1.19 R_M, 0.0047)$, which is almost identical to the Mars
207 Express *Han et al.* [2014] derived results values $(0.01 R_M, 1.19 R_M, 0.005)$. The average
208 location of the PEB is thus very close to a circle (red line) centered on the planet cen-
209 ter, as can be expected for the innermost plasma boundary. The closer the boundary, the
210 lower the eccentricity : the MPB and Bow-Shock best conic fits respectively correspond
211 to eccentricities of 0.92/0.90 (*Edberg et al.* [2008] / *Vignes et al.* [2002]) and 1.05/1.03
212 (*Edberg et al.* [2008] / *Vignes et al.* [2002] and *Trotignon et al.* [2006]).

213 **2.2 Solar zenith angle and local time variability**

214 Figures 3 and 4 show the altitude, solar zenith angle (SZA) and local time (LT) vari-
215 ability of the 3022 photoelectron line crossings determined during the two first years of
216 the MAVEN mission. The photoelectron line crossings beyond 90° SZA or below the ex-
217 treme ultraviolet terminator (for a lower limit altitude of 140 km) are not a priori consid-
218 ered as real PEB crossings, even if some of them could be included as well. Until 30°
219 SZA, the median altitude of the PEB crossings decreases at first, and then increases until
220 a constant value below 600 km from 55° SZA. The increase of the PEB altitude is ex-
221 pected towards the terminator, since the draped field lines induce an increase of the MPB
222 altitude with SZA, but larger altitudes closer to noon are unexpected. Moreover, the me-
223 dian local time variability in the MSO frame shows an unexpected and significant asym-
224 metry, with a minimum altitude displaced with respect to noon, whereas the draping topol-
225 ogy can be considered as symmetric. Where do these unexpected features come from ?
226 One can mention that a separation of the datasets into northern hemisphere and southern
227 hemisphere observations (not shown) reveals higher altitudes in the south than in the north
228 (presumably due to an enhanced crustal field pressure, see next section), except again near
229 noon (in both SZA and LT) where the trend is reversed.

230 Since the draping of the IMF around Mars - and the Martian interaction with the
231 solar wind in general - is known to depend significantly on the clock angle of the IMF
232 [*Carlsson et al.*, 2008], the PEB is expected to depend on it as well. Moreover, the so-
233 lar wind velocity compared to the orbital velocity of the planet around the Sun induces
234 a small but non negligible aberration angle (of a few degrees). We thus recalculated the
235 SZA and LT values in the MSE frame that also includes a 4° aberration angle, based on
236 the solar wind velocity and magnetic field parameters provided by the MAVEN SWIA
237 and MAG instruments at each orbit [*Halekas et al.*, 2017]. The resulting new LT median

238 variability (red line) shows a much more symmetric behavior : the PEB is thus strongly
239 organized by the solar wind magnetic field direction, whose variability induces a continu-
240 ous rotation of the draping around the X axis and thus a reorganization in terms of local
241 time. One can also mention that the latitudinal variability of the PEB (not shown) is much
242 more homogeneous in this modified MSE frame than in the MSO frame.

243 However, the SZA variability is obviously only slightly influenced by a small aber-
244 ration angle, so that the unexpected high altitude PEB crossings near noon need another
245 explanation. Figure 5 shows the SZA variability of the crustal magnetic field (at a con-
246 stant altitude of 400 km ; *Morschhauser et al.* [2014]) and solar wind dynamic pressure
247 at the times of the photoelectron line crossings. A clear bias thus appears in our dataset
248 close to noon, with low solar wind dynamic pressures and high crustal magnetic field val-
249 ues. As will be detailed in the next section, both the solar wind and crustal magnetic field
250 pressures are important drivers for the PEB location, since the pressure will push from
251 above (for the solar wind) or below (for crustal fields) the draping magnetic field topol-
252 ogy, and modify the location where the upward moving photoelectrons will encounter the
253 draped open field lines to get eventually convected toward the tail. A combination of (rel-
254 ative) low solar wind dynamic pressure and strong crustal field pressure will thus induce
255 high altitudes for the PEB as observed in our dataset.

256 **3 The parameters of influence for the PEB : solar wind dynamic and crustal mag-** 257 **netic fields pressures**

258 The conic fitting of the dayside PEB crossings leads to a nearly circular shape of the
259 boundary. Nonetheless, from now on we will only use the extrapolated terminator distance
260 (i.e. $r_i(1 + e * \cos(\theta_i))$) or altitude of the PEB to remove the average SZA variability of the
261 PEB altitude, following previous works on the MPB or bow shock (*Crider et al.* [2003] or
262 *Edberg et al.* [2008]).

263 **3.1 The influence of the crustal magnetic field and solar wind dynamic pressure**

264 The influence of the crustal field intensity on the PEB altitude is shown in figure
265 6, where the estimated terminator altitude is given as a function of the longitude in the
266 geographical IAU frame. This frame is fixed to the planet, with the strongest crustal fields
267 region in the southern hemisphere at longitudes between 120 and 240 deg. The dataset is
268 separated into longitude and latitude regions to separate the strong and weak crustal field

269 regimes, as defined by *Edberg et al.* [2008], with the strong fields in the following ranges :
270 longitude from 0 to 120 deg and latitude from -45 to 45 deg, longitude from 120 to 240
271 deg and latitude from -90 to 0 deg, and longitude from 240 to 360 deg and latitude from
272 -45 to 45 deg.

273 The median altitudes are systematically higher for the strong crustal field regime
274 than for the low crustal field regime, by about 100 km or even 140 km in 120 to 240 deg
275 longitude region where the strongest crustal fields are located. *Edberg et al.* [2008] ob-
276 tained very similar results for the influence of crustal fields on the MPB and bow shock
277 position, with the largest influence in the middle longitude range as well, with an alti-
278 tude variation that is all the larger than the boundary is far : up to ~ 400 km and ~ 0.48
279 R_M for respectively the MPB and bow shock. One can also note that an IAU mapping of
280 the PEB terminator altitude from our dataset gives a good correlation with the location of
281 crustal field sources.

282 The combined influence of the solar wind dynamic pressure and crustal magnetic
283 field is shown in figure 7. Despite a strong dispersion and a limited number of PEB cross-
284 ings at high solar wind dynamic pressure values, the PEB terminator altitude clearly de-
285 creases while the solar wind dynamic pressure increases, with a median altitude decreas-
286 ing from ~ 700 km to ~ 500 km. The separation between weak and strong crustal field
287 crossings is also clear, with few high altitude crossings located above weak crustal field
288 regions. Power law fits were performed of the form $d_{termPEB} = a * P_{SW}^b$ with $d_{termPEB}$
289 terminator distance of the PEB in R_M and P_{SW} the solar wind dynamic pressure, for all
290 crossings together (magenta line in the figure) or by separating weak (blue line) and strong
291 (red line) crustal field crossings. The results are the following : $(a, b) \approx (3.60, -0.034)$
292 for all crossings ; $(3.59, -0.034)$ for crossings above weak crustal fields ; $(3.61, -0.039)$
293 for crossings above weak crustal fields. The influence of the solar wind dynamic pressure
294 is thus on average 40% smaller than on the MPB, for which the power law index value
295 was estimated at about -0.055 [*Crider et al.*, 2003], which is expected since the PEB is
296 located closer to the planet. Even if the dispersion is very large, we may add that the in-
297 fluence of both the solar wind dynamic pressure and crustal magnetic field pressure are
298 statistically very significant (assuming power laws), with Fisher tests [*Box*, 1953] providing
299 risks - i.e. probabilities that the influence is not real - of about 10^{-29} and 10^{-18} respec-
300 tively. These results are in agreement with a confinement of the atmosphere by the solar
301 wind, that induces a draping of the IMF closer to the planet and thus pushes the PEB to

302 lower altitudes, except when strong crustal fields locally act from below against this inci-
303 dent pressure.

304 3.2 Comparing the parameters of influence

305 Figure 8 shows the compared influence on the PEB terminator altitude of a num-
306 ber of parameters: extreme ultraviolet fluxes, solar zenith angle, local time, crustal mag-
307 netic field pressure, as well as solar wind dynamic pressure, density, velocity and magnetic
308 field. We shall mention the EUV fluxes are derived from the FISM model (*Chamberlin*
309 *et al.* [2007] ; available on the CDPP/AMDA database) at the 30.4 nm solar spectrum line
310 which is the source of the 20 – 30 eV photoelectrons. Each set of parameters was then
311 separated into low (below the median value of the parameter) and high (above the me-
312 dian value of the parameter) subsets of data to allow for a convenient comparison among
313 the various parameters of influence. The median altitudes of the "low" and "high" sub-
314 sets are then determined for each parameter. The standard deviation of the median value
315 ($\frac{\sigma}{\sqrt{N}}$; σ standard deviation and N number of values) was shown in the figure instead of
316 the classical standard deviation for a better visibility (σ is very large, about 200 km). We
317 shall mention that in this figure we only considered the crossings for which all parameters
318 were available (the solar wind parameters being available for only a part of them), which
319 reduces the dataset to 795 PEB crossings. However, the relative importance of the param-
320 eters keeps very similar if all crossings are considered for the EUV, LT, SZA and crustal
321 field parameters.

322 The PEB terminator altitude thus increases with (by decreasing importance) increas-
323 ing crustal magnetic field pressure, decreasing solar wind dynamic pressure, increasing
324 local time, increasing EUV fluxes and decreasing SZA and IMF. The two major parame-
325 ters of influence are by far the solar wind dynamic and crustal magnetic field pressures,
326 with a variation reaching 150 km of difference between the low and high median values.

327 More precisely, the low solar wind density seems even more efficient than a low
328 velocity to cause an increase in the PEB altitude. *Ramstad et al.* [2015] showed that low
329 solar wind densities lead to larger ion escape rates according to Mars-Express ASPERA-3
330 data, since the atmosphere expands, giving more space and time for ionospheric plasma
331 to accelerate, which leads to larger escape rates during the rarefaction (i.e. low SW den-
332 sity) events following the strong solar wind disturbances. We will discuss in section 4 how

333 the solar wind dynamic pressure will impact the escape rates through the variable PEB
334 altitude.

335 The influence of the other parameters - EUV, SZA and LT - is less clear, depends
336 on the frame considered (for the LT influence in MSO vs MSE) or on cross correlations
337 biases with the major drivers (for SZA near noon, as detailed above), even if the risks of
338 artificial correlations as determined from Fisher's tests are always below 1% except for the
339 SZA influence (risk of $\approx 2\%$). Regarding the EUV influence, we point out that if EUV
340 is a major driver for the photoelectron fluxes (*Trantham et al.* [2011] ; *Xu et al.* [2015])
341 through the production mechanisms, its influence on the PEB should be less strong (e.g.
342 the MGS data could not see any EUV influence on the ionopause [*Mitchell et al.*, 2001]).
343 The EUV influence corresponds to an enhanced thermal pressure that will act against the
344 solar wind confinement and thus push the draping of the IMF.

345 **4 Discussion on the photoelectron escape**

346 The PEB altitude is strongly influenced by the incident solar wind dynamic pressure
347 that confines more or less the Martian ionosphere and that thus drives the location of the
348 IMF draping around the planet. As shown in figure 9 and explained below, the solar wind
349 will consequently have a strong impact on the transport of the photoelectrons from the
350 dayside to the tail region and eventually on the estimated escape rates derived.

351 In this figure, we assumed a continuous detection of 20 – 30 eV photoelectrons
352 from the inbound to outbound crossings of the photoelectron line. This assumption is in-
353 accurate in the nightside region where a lot of electron depletions are observed, but it is
354 mostly true otherwise, except at intermittent times in the non-collisional regions due to the
355 strong plasma dynamics (mixing of several populations, accelerated particles, etc.). We
356 separated the time intervals into four categories, based on the value of the solar wind dy-
357 namic pressure at the times considered, and superimposed the crossings on the figure in
358 the following order: very low, low, high, very high. The low and very low SW pressures
359 are hidden behind the high and very SW pressures close to the planet, but extend further
360 than these. The photoelectron detection thus appears more and more confined close to the
361 planet when higher solar wind dynamic pressure values are observed, not only on the day-
362 side but also at terminator where the photoelectrons are on the way to escape down to the
363 tail.

364 The PEB altitude is raised by low solar wind dynamic pressure conditions, leading
365 to access to higher altitudes on the dayside for the photoelectrons, and thus transport along
366 draped field lines toward the tail at higher altitudes as well. Overall, the photoelectron
367 escape will not necessarily increase due to low solar wind dynamic pressure conditions,
368 but the tail cross section to be considered for deriving escape rates increases. *Frahm et al.*
369 [2010] provided the only known escape rates of photoelectrons ($3.14 \pm 1.78 * 10^{23}$ elec-
370 trons/ s), and thus of corresponding ionospheric ions - assuming they escape at the same
371 rate as the electrons, which may be overestimated if their large gyroradii make them im-
372 pact the dense atmosphere -, based on a average escape flux measured and a constant an-
373 nular cross section of $1.16 * 10^{18} \text{ cm}^2$. This annular cross section was derived at $X = -1.5$
374 R_M , with a minimum distance to the X axis of 2850 km (no escaping photoelectrons at
375 Mars were observed closer to the X axis) and an external limit at 6700 km. However, our
376 results show that the cross section to be considered for deriving escape rates is not a con-
377 stant and will strongly depend on the PEB altitude on the dayside and thus in particular
378 on the solar wind dynamic (and crustal magnetic field) pressure. Assuming sketched limits
379 for low and high PEB altitudes (black and red lines in figure 9), corresponding to about
380 200 km of difference near noon, and by extrapolating their shape to the tail until $X = -1.5$
381 R_M , this will induce a variation of about 50% of the escape cross section. When escape
382 rates are derived from single point in situ flux measurements, one should thus keep in
383 mind that not only the measured local fluxes vary temporally and spatially, but the escape
384 area (i.e. the cross section to be used) will significantly vary with time and depend on the
385 dayside conditions. We mention that deriving MAVEN escape rates is beyond the scope of
386 this paper, since it needs the quantitative analysis of the photoelectron peaks in the energy
387 spectra (whereas we only focus on the PEB crossings here), but we plan to further inves-
388 tigate this in the future to analyze the variability of the escape rates during the MAVEN
389 mission (with an average value that could be, or not, close to earlier estimates).

390 **5 Characteristics around the boundary**

391 Beyond the knowledge of the location and of the variability of the boundary, it is
392 essential to better understand its nature and characteristics, therefore we examine the evo-
393 lution of a number of parameters around it. Figure 10 provides the average evolution of
394 the 23 – 29 eV photoelectron integrated differential fluxes (panel a), electron density (panel
395 c), electron differential fluxes at ~ 25 and ~ 130 eV (panel c), as well as information on

396 the pitch angle distributions (panel b) and several magnetic field characteristics (panels d
397 e f), as a function of the altitude around the boundary. The altitude 0 in the figure thus
398 corresponds to the altitude of each individual PEB crossing, while positive and negative
399 values correspond respectively to altitudes above and below the crossing. Such a figure
400 hides the various trajectories of the spacecraft, with in particular the altitude variation be-
401 ing different from one orbit to another, but it allows us to compare crossings occurring at
402 different times and altitudes, by normalizing some of the parameters to avoid their strong
403 temporal and/or spatial dynamics to hide the average characteristics of the PEB (e.g. for
404 the electron density, or total magnitude of the magnetic field).

405 We considered all MAVEN SWEA (with ~ 4 s time resolution) and MAG (with
406 ~ 2 s time resolution) data at ± 300 s around the time of each of the 1696 PEB crossings
407 available. Median (for panels a d e f) or average (for panels b and c) parameter values
408 were then calculated for each 20 km altitude bin around the crossings, which leads to a
409 maximum altitude range of 700 km. We however removed the data below -200 km since
410 the average altitude actually increases below this limit, which would induce a bias for the
411 interpretation if these data were kept. The standard deviation of the mean ($\frac{\sigma}{\sqrt{N}}$) is also
412 shown for each parameter as an errorbar. In panels a, d, e, f, we also considered three
413 different profiles to identify the influence of the crustal fields: one for all PEB crossings
414 (black line), and two for low (blue line) and high (red line) crustal field conditions at the
415 crossings. These low/high conditions are determined by the 25% percentiles of the cross-
416 ings with the lowest and highest values of the *Morschhauser et al.* [2014] modeled crustal
417 magnetic field values at 400 km altitude at the time of crossings.

418 Panel a) provides the integrated 20 – 30 eV photoelectron flux, normalized by the
419 flux at the time of each PEB crossing. Following the approach of *Frahm et al.* [2010], we
420 integrated, for each time step, the photoelectron flux after removing the background spec-
421 trum (i.e. a power law fit) from 17.2 to 34.7 eV to extract the peak photoelectron fluxes
422 only. Several tries were made with various energy ranges considered, leading to no sig-
423 nificant qualitative change in the results, and the energy of the peak is very stable on the
424 dayside. Above the PEB, the photoelectrons are by definition essentially absent, so that the
425 fluxes should not be considered from about 50 km above the PEB (gray area), since they
426 correspond to fluxes of magnetosheath electrons. The flux of upward moving pho-
427 toelectrons gradually decreases when approaching the boundary, before a large drop in a
428 ~ 100 km altitude shell centered on the PEB location, and ultimately they disappear. We

429 also find the presence of higher fluxes in the -200 to -100 *km* range when weak crustal
430 fields are present, which may be related to an easier access of photoelectrons to altitudes
431 above the photoelectron exobase ($\approx 145 - 165$ *km* altitude, see *Xu et al.* [2016b]) in the
432 absence of strong horizontal closed crustal magnetic fields.

433 The median profiles of the magnetic field characteristics (local rotation every 4 sec-
434 onds, panel b ; elevation angle, panel c ; magnitude of the field measured normalized by
435 the value at the PEB) suggest the following average behavior from above to below the
436 PEB. The magnetic field first drapes (and thus rotates less and less) and piles-up (the to-
437 tal field increases) at altitudes above the PEB, which is consistent with the Magnetic-Pile
438 up Region (MPR) characteristics, and is consistent with the fact that most data points con-
439 sidered here are located below the nominal Magnetic Pile-Up Boundary location. The ro-
440 tation of the field decreases towards lower altitudes, as does the magnetic field elevation
441 angle that reaches a constant minimum value about 250 *km* above the PEB location. The
442 situation seems however different with strong crustal fields: the interaction between up-
443 stream and crustal topologies induces on average an increase of the elevation angle ~ 150
444 *km* above the PEB (the influence of crustal fields may also be seen at the same time on
445 the field rotation with a separation between low and high crustal field profiles). 50 *km*
446 above the PEB, while the photoelectron fluxes appear and strongly increase, the local rota-
447 tion of the magnetic field increases slightly, and reaches a peak exactly at the PEB in the
448 presence of crustal fields (for this case the PEB marks a transition between two different
449 configurations of the magnetic field, the draped field above and the crustal field below).
450 We note that the absolute values of the rotation are small, which is due to the time resolu-
451 tion considered (4 *s*, a poorer resolution would lead to larger rotation angles). At the same
452 time (i.e. 50 *km* or less above the PEB) the magnetic elevation angle slightly increases
453 as well (all the more in the presence of crustal fields) and the total field keeps constant
454 around the boundary (typical for the end of the MPR). Then, below the PEB, the rotation
455 of the field stays small while the elevation angle slightly increases (with a more noisy be-
456 havior in the presence of crustal fields, due to the variable local topology) and the field
457 magnitude decreases / increases in the absence / presence of crustal fields.

458 Panel b) shows information regarding the pitch angle distribution of $23 - 29$ *eV* elec-
459 trons around the PEB (the most appropriate energy bin to investigate $20 - 30$ *eV* photoelec-
460 trons with the Pitch Angle Distribution (PAD) mode of the MAVEN SWEA instrument).
461 The red line provides the ratio between the maximum parallel or anti-parallel (maximum

value among either the $0 - 45^\circ$ or $135 - 180^\circ$ pitch angle ranges) and perpendicular ($45 - 135^\circ$) differential fluxes. The green and black lines give respectively the probability of "loss cone" and "field aligned" pitch angle distributions for the $0 - 90^\circ$ range. We defined these categories based on an approach similar to *Brain et al.* [2007]: each half of a PAD is taken separately ($0-90^\circ$ and $90-180^\circ$), and the standard deviation of fluxes of each half is calculated among the angular bins ; the flux at 90° pitch angle is then compared to the most field-aligned flux for the spectrum (here at least $\leq 30^\circ$ or $\geq 150^\circ$ to avoid too narrow PADs) ; PAD spectra are separated according to whether the perpendicular flux at 90° exceeds the field-aligned flux by more than one standard deviation ("loss cone") or whether the field-aligned flux exceeds the perpendicular flux by more than one standard deviation ("field-aligned"). The rest of the spectra correspond to either isotropic or conic / anti-conic spectra (not shown). We shall mention that only the qualitative behavior is discussed here, since changing the definition of the parameters modifies the absolute probabilities of each configuration.

Globally, the $23 - 29$ eV electrons - i.e. essentially photoelectrons below the PEB, magnetosheath electrons above it - PADs are more in a field aligned configuration than in a loss cone configuration, except at -140 km below the PEB where both configurations have a similar probability. From about -200 km below the PEB until the boundary, the loss cone and field-aligned probabilities vary from respectively between 0.3 and 0.4 and between 0.4 and 0.5. The loss cone and field-aligned probabilities then abruptly decrease / increase from the PEB (or slightly below it) to about 50 km above it, before they keep stable at respectively ≈ 0.25 and ≈ 0.6 (with a slight continuous increase though). This change of PAD configuration at the PEB is clearly confirmed by the ratio between the maximum parallel (or anti-parallel) and the perpendicular fluxes, which is roughly constant below and above the PEB but strongly increases from the PEB to 50 km above it (from 1.4 to 1.6), revealing an even more field aligned configuration above than below the boundary (where the PADs are already more field aligned, with a ratio always above 1). As expected, the PADs are more in a field-aligned configuration (thus with more electrons on open field lines, at one end or both) than in a loss cone configuration (closed field lines). We are indeed looking at relatively high altitudes compared to the photoelectron exobase [*Xu et al.*, 2016b]: 71/86 % of the time steps considered correspond to altitudes above $300/400$ km respectively, with an average altitude reaching a minimum of 400 km (at about -150 km below the PEB, which explains the close green and black curves at

495 this location). Moreover, plotting the probability of closed (loss cone + isotropic + conic
496 PADs) and open (field-aligned + anti-conic) fields configurations as a function of absolute
497 altitude (not referenced to the PEB level ; plot not shown) reveals an expected continuous
498 decrease and increase versus altitude for these respective configurations, with equal proba-
499 bilities at about 300 – 400 km. These observations are in agreement with the recent results
500 by *Xu et al.* [2017] who investigated in details the low altitude topology and electron pitch
501 angle distributions based on the shape parameter technique. This technique (see details in
502 *Xu et al.* [2017]) is based on a parameter whose value determines the nature of the elec-
503 tron spectra (photoelectrons or solar wind) after a comparison between measured spectra
504 and a ionosphere reference spectrum (that includes the 20 – 30 eV peaks and the sharp
505 drop at 60 – 70 eV). The authors showed that closed field lines are mostly observed at
506 low altitudes (and above crustal fields), and that above 400 km altitudes the field lines are
507 mostly open and draped around the planet.

508 Panel (c) shows the mean absolute differential fluxes of 23 – 29 eV (black lines) and
509 118 – 149 eV (green lines) electrons around the PEB, the low energy range corresponding
510 to either photoelectrons (mostly below the PEB) or magnetosheath electrons (mostly above
511 the PEB), while the high energy range corresponds essentially to magnetosheath electrons
512 only and keeps a good signal to noise ratio compared to higher energy ranges. The PEB
513 appears as a clear transition between the photoelectron dominated and magnetosheath
514 electron dominated regions, with magnetosheath electron fluxes dropping above the PEB
515 (by up to one order of magnitude in about 50 – 100 km for the highest energies), while the
516 photoelectrons fluxes (i.e. 23 – 29 eV electrons below the PEB) appear and increase below
517 the boundary (since the photoelectron source region is at low altitudes). We shall mention
518 that the profiles are similar for all crustal field conditions. Meanwhile, a strong change in
519 the density profile occurs at the PEB altitude, with a clear and large increase of the gradi-
520 ent with altitude from above to below the PEB. Moreover, one can note that plotting the
521 absolute densities (not normalized to 1 at the PEB ; not shown) as a function of altitude
522 versus the PEB confirms our conclusions with the same strong change of slope above the
523 PEB. Finally, in addition to this observation of smaller density gradients above the PEB
524 (and not larger gradients as may be used to define the ionopause), the 1000 cm⁻³ density
525 level used by *Han et al.* [2014] to define the ionopause level is located in our dataset at
526 ~ 440 km, which is similar to the Mars Express results (and ~ 200 km below our average
527 PEB altitude) : these results thus confirm that the PEB and ionopause (as defined by large

528 density gradients or the 1000 cm^{-3} density level) are not located at the same altitude on
529 average. We shall mention that the normalization of both the density and altitude axes of
530 panel c make it impossible to add the location of the ionopause on the same figure even
531 as defined from a constant density level.

532 The average variability of plasma and magnetic fields around the PEB altitude thus
533 reveals several characteristics :

- 534 • the 20 – 30 eV photoelectron flux first gradually decreases from below the PEB ,
535 followed by a strong decrease around the PEB over an altitude shell 'thickness' of
536 the order of 100km altitude until photoelectrons disappear
- 537 • the magnetic field is characteristic for the magnetic pile-up region above the PEB,
538 with a strong (decreasing towards the PEB) rotation of the field and a decreasing
539 elevation until the field gets draped ; the field magnitude increases linearly until it
540 gets stable around the PEB, where a local increase of rotation and elevation is ob-
541 served ; finally, the crustal fields determine the low altitude topology (and influence
542 the topology at least until 150 km above the PEB)
- 543 • the pitch angle distributions of 23 – 29 eV electrons (i.e. photoelectrons below
544 the PEB) show a steep increase of the ratio between parallel (or anti-parallel, the
545 maximum value being considered) and perpendicular fluxes at the PEB, and a in-
546 crease/decrease of the probability for field aligned / loss cone PADs at the same
547 time, even if the PADs reveal more open field lines than closed fields lines at the
548 altitudes considered in our study (in agreement with *Xu et al.* [2017])
- 549 • the electron fluxes reveal a steep increase of high energy electrons (i.e. magne-
550 tosheath type electrons) above the PEB and a smaller decrease of 25 eV electron
551 fluxes, while the slope of the density profile strongly increases at the PEB ; the
552 PEB is thus on average different from an ionopause defined by either a stronger
553 density depletion or by a 1000 cm^{-3} density level [*Han et al.*, 2014] (which actu-
554 ally also occurs about 200 km below the PEB on the MAVEN data). The PEB thus
555 appears as a flux and density transition region between ionospheric and magne-
556 tosheath electrons.

557 Overall, these characteristics are consistent with the classical picture of the PEB as
558 the location where photoelectrons, after their upward transport above the exobase (mod-
559 ified by the magnetic topology, in particular crustal fields), encounter open draped field

560 lines, with more field aligned PADs and get convected towards the tail and eventually es-
561 cape. However, beyond the coherent average profiles discussed in this section, a large dis-
562 persion appears when individual crossings are analyzed. The dispersion (ratio between
563 standard deviation and mean values) is most often above one for all particles parameters
564 (photoelectron flux, electron fluxes and density, pitch angle profiles) and at all altitudes.
565 The small errorbars of figure 10 actually correspond to the standard deviation of the mean
566 (i.e. much smaller than the nominal standard deviation). In the future, individual cross-
567 ings will be investigated in more details to better understand the large dynamics beyond
568 the global trends discussed above.

569 **6 Conclusions**

570 The characterization of the plasma boundaries at Mars and their difference has been
571 a matter of debate for many years. In particular, the photoelectron boundary (PEB) discov-
572 ered by Mars Global Surveyor and defined by the disappearance of ionospheric photoelec-
573 trons, still remains poorly understood. We provide in this paper a detailed description of
574 the PEB based on a manual detection of almost 1700 boundary crossings from MAVEN
575 data before May 2016. We thus determined its shape, its parameters of influence, the vari-
576 ability of several parameters (magnetic field, photoelectron fluxes, etc.) in the vicinity of
577 the boundary, and its influence on the plasma escape fluxes. Our main conclusions are the
578 following.

- 579 1. First, the PEB appears approximately as a circular boundary ($e = 0.0047$) with a
580 highly variable altitude that is strongly related to the draping of the IMF around
581 the planet, and mostly depends on the solar wind dynamic and crustal magnetic
582 field pressures (more than extreme ultraviolet fluxes or solar zenith angle and local
583 time). These pressures will push from above (for the solar wind) or below (for the
584 crustal fields) the draping magnetic field topology, and thus modify the location
585 where the upward moving photoelectrons will encounter the draped open field lines
586 to get eventually convected toward the tail.
- 587 2. Second, we show how the variable PEB altitude on the dayside, due to several
588 drivers, will allow the access of photoelectrons to variable altitudes towards the
589 terminator and thus affect their transport along draped field lines toward the tail and
590 strongly modify (up to $\sim 50\%$) the tail cross section to be considered for deriving
591 escape rates of photoelectrons (and associated ions assuming neutrality). When es-

592 cape rates are derived from single point in situ flux measurements, the temporal
593 and spatial variations of the dayside PEB altitude will thus determine the escape
594 cross section to be considered.

595 3. Finally, the detailed analysis of plasma and magnetic field characteristics around the
596 PEB crossings shows that the boundary is not always sharp, and is characterized on
597 average by :

- 598 • a gradual decrease of the photoelectron flux much before the PEB and a more
599 steep decrease around it over an altitude "thickness" of the order of 100 *km*
- 600 • a magnetic field topology typical for the end of the Magnetic Pile Up Region
601 above it, with also a locally increased rotation and elevation angle of the field at
602 the PEB all the more in the presence of crustal field sources
- 603 • more field aligned fluxes above than below the boundary, despite a more "open"
604 than "closed" field configuration usually much below the PEB
- 605 • a clear change of altitude slopes for both the electron fluxes (in particular for
606 high energy electrons) and total density ; the density slope indeed decreases
607 from below to above the boundary, the PEB being thus different from the ionopause
608 if defined by a stronger density slope, and more precisely located ~ 200 *km* be-
609 low the PEB if defined as the 1000 cm^{-3} density level

610 However, beyond these average characteristics of the PEB, a large dispersion appears
611 when individual crossings are analyzed and should be investigated in the future. Further-
612 more, a more detailed understanding of the various plasma boundaries (MPB/IMB, pres-
613 sure boundary, ion composition boundary, ionopause...) and of the physical processes link-
614 ing them will need future common work, by taking advantage of the complete particles
615 and fields package of the MAVEN mission.

616 **Acknowledgments**

617 This work was supported by the French space agency CNES for the observations obtained
618 with the SWEA instrument embarked on MAVEN. The authors acknowledge the sup-
619 port of the MAVEN instrument and science teams, as well as are the CDPP/AMDA team
620 (<http://amda.cdpp.eu>) and Emmanuel Penou for providing support with data analysis tools.
621 The MAVEN data are taken from the Berkeley database with the "spdsoft" software.

References

- Barabash, S., R. Lundin, H. Andersson, K. Brinkfeldt, A. Grigoriev, H. Gunell, M. Holmström, M. Yamauchi, K. Asamura, P. Bochsler, P. Wurz, R. Cerulli-Irelli, A. Mura, A. Milillo, M. Maggi, S. Orsini, A. J. Coates, D. R. Linder, D. O. Kataria, C. C. Curtis, K. C. Hsieh, B. R. Sandel, R. A. Frahm, J. R. Sharber, J. D. Winningham, M. Grande, E. Kallio, H. Koskinen, P. Riihelä, W. Schmidt, T. Säles, J. U. Kozyra, N. Krupp, J. Woch, S. Livi, J. G. Luhmann, S. McKenna-Lawlor, E. C. Roelof, D. J. Williams, J.-A. Sauvaud, A. Fedorov, and J.-J. Thocaven (2006), The Analyzer of Space Plasmas and Energetic Atoms (ASPERA-3) for the Mars Express Mission, *Space Science Reviews*, 126(1), 113–164, doi:10.1007/s11214-006-9124-8.
- Bertucci, C., C. Mazelle, D. H. Crider, D. L. Mitchell, K. Sauer, M. H. Acuña, J. E. P. Connerney, R. P. Lin, N. F. Ness, and D. Winterhalter (2004), MGS MAG/ER observations at the magnetic pileup boundary of Mars: draping enhancement and low frequency waves, *Advances in Space Research*, 33, 1938–1944, doi:10.1016/j.asr.2003.04.054.
- Box, G. (1953), Non-normality and tests on variances, *Biometrika*, 40(3-4), 318–335, doi:10.1093/biomet/40.3-4.318.
- Brain, D. A., R. J. Lillis, D. L. Mitchell, J. S. Halekas, and R. P. Lin (2007), Electron pitch angle distributions as indicators of magnetic field topology near Mars, *Journal of Geophysical Research (Space Physics)*, 112, A09201, doi:10.1029/2007JA012435.
- Brain, D. A., S. Barabash, S. W. Bougher, F. Duru, B. M. Jakosky, and R. Modolo (2017), *Solar Wind Interaction and Atmospheric Escape*, p. 433–463, Cambridge Planetary Science, Cambridge University Press, doi:10.1017/9781139060172.015.
- Carlsson, E., D. Brain, J. Luhmann, S. Barabash, A. Grigoriev, H. Nilsson, and R. Lundin (2008), Influence of IMF draping direction and crustal magnetic field location on Martian ion beams, *Planetary and Space Science*, 56(6), 861 – 867, doi: http://dx.doi.org/10.1016/j.pss.2007.12.016, mars Express/Venus Express.
- Chamberlin, P. C., T. N. Woods, and F. G. Eparvier (2007), Flare Irradiance Spectral Model (FISM): Daily component algorithms and results, *Space Weather*, 5, S07005, doi:10.1029/2007SW000316.
- Coates, A. J., S. M. E. Tsang, A. Wellbrock, R. A. Frahm, J. D. Winningham, S. Barabash, R. Lundin, D. T. Young, and F. J. Crary (2011), Ionospheric photoelectrons: Comparing Venus, Earth, Mars and Titan, *Planetary and Space Science*, 59,

1019–1027, doi:10.1016/j.pss.2010.07.016.

Coates, A. J., A. Wellbrock, R. A. Frahm, J. D. Winningham, A. Fedorov, S. Barabash, and R. Lundin (2015), Distant ionospheric photoelectron energy peak observations at Venus, *Planetary and Space Science*, *113*, 378–384, doi:10.1016/j.pss.2015.02.003.

Connerney, J. E. P., J. Espley, P. Lawton, S. Murphy, J. Odom, R. Oliverson, and D. Sheppard (2015), The MAVEN Magnetic Field Investigation, *Space Science Reviews*, *195*, 257–291, doi:10.1007/s11214-015-0169-4.

Crider, D. H., D. Vignes, A. M. Krymskii, T. K. Breus, N. F. Ness, D. L. Mitchell, J. A. Slavin, and M. H. Acuña (2003), A proxy for determining solar wind dynamic pressure at Mars using Mars Global Surveyor data, *Journal of Geophysical Research (Space Physics)*, *108*, 1461, doi:10.1029/2003JA009875.

Dubinin, E., M. Fränz, J. Woch, E. Roussos, S. Barabash, R. Lundin, J. D. Winningham, R. A. Frahm, and M. Acuña (2006), Plasma Morphology at Mars. Aspera-3 Observations, *Space Science Reviews*, *126*, 209–238, doi:10.1007/s11214-006-9039-4.

Edberg, N. J. T., M. Lester, S. W. H. Cowley, and A. I. Eriksson (2008), Statistical analysis of the location of the martian magnetic pileup boundary and bow shock and the influence of crustal magnetic fields, *Journal of Geophysical Research: Space Physics*, *113*(A8), n/a–n/a, doi:10.1029/2008JA013096, a08206.

Frahm, R. A., J. R. Sharber, J. D. Winningham, P. Wurz, M. W. Liemohn, E. Kallio, M. Yamauchi, R. Lundin, S. Barabash, A. J. Coates, D. R. Linder, J. U. Kozyra, M. Holmström, S. J. Jeffers, H. Andersson, and S. McKenna-Lawler (2006), Locations of Atmospheric Photoelectron Energy Peaks Within the Mars Environment, *Space Science Reviews*, *126*, 389–402, doi:10.1007/s11214-006-9119-5.

Frahm, R. A., J. R. Sharber, J. D. Winningham, R. Link, M. W. Liemohn, J. U. Kozyra, A. J. Coates, D. R. Linder, S. Barabash, R. Lundin, and A. Fedorov (2010), Estimation of the escape of photoelectrons from Mars in 2004 liberated by the ionization of carbon dioxide and atomic oxygen, *Icarus*, *206*, 50–63, doi:10.1016/j.icarus.2009.03.024.

Halekas, J. S., S. Ruhunusiri, Y. Harada, G. Collinson, D. L. Mitchell, C. Mazelle, J. P. McFadden, J. E. P. Connerney, J. R. Espley, F. Eparvier, J. G. Luhmann, and B. M. Jakosky (2017), Structure, dynamics, and seasonal variability of the Mars-solar wind interaction: MAVEN Solar Wind Ion Analyzer in-flight performance and science results, *Journal of Geophysical Research (Space Physics)*, *122*, 547–578, doi:10.1002/2016JA023167.

688 Han, X., M. Fraenz, E. Dubinin, Y. Wei, D. J. Andrews, W. Wan, M. He, Z. J. Rong,
689 L. Chai, J. Zhong, K. Li, and S. Barabash (2014), Discrepancy between ionopause and
690 photoelectron boundary determined from Mars Express measurements, *"Geophysical
691 Research Letters"*, *41*, 8221–8227, doi:10.1002/2014GL062287.

692 Jakosky, B. M., R. P. Lin, J. M. Grebowsky, J. G. Luhmann, D. F. Mitchell, G. Beu-
693 telschies, T. Priser, M. Acuna, L. Andersson, D. Baird, D. Baker, R. Bartlett, M. Benna,
694 S. Bougher, D. Brain, D. Carson, S. Cauffman, P. Chamberlin, J.-Y. Chaufray,
695 O. Cheatom, J. Clarke, J. Connerney, T. Cravens, D. Curtis, G. Delory, S. Demcak,
696 A. DeWolfe, F. Eparvier, R. Ergun, A. Eriksson, J. Espley, X. Fang, D. Folta, J. Fox,
697 C. Gomez-Rosa, S. Habenicht, J. Halekas, G. Holsclaw, M. Houghton, R. Howard,
698 M. Jarosz, N. Jedrich, M. Johnson, W. Kasprzak, M. Kelley, T. King, M. Lankton,
699 D. Larson, F. Leblanc, F. Lefevre, R. Lillis, P. Mahaffy, C. Mazelle, W. McClintock,
700 J. McFadden, D. L. Mitchell, F. Montmessin, J. Morrissey, W. Peterson, W. Possel, J.-A.
701 Sauvaud, N. Schneider, W. Sidney, S. Sparacino, A. I. F. Stewart, R. Tolson, D. Tou-
702 blanc, C. Waters, T. Woods, R. Yelle, and R. Zurek (2015), The Mars Atmosphere
703 and Volatile Evolution (MAVEN) Mission, *"Space Science Reviews"*, *195*, 3–48, doi:
704 10.1007/s11214-015-0139-x.

705 Liemohn, M. W., R. A. Frahm, J. D. Winningham, Y. Ma, S. Barabash, R. Lundin,
706 J. U. Kozyra, A. F. Nagy, S. M. Bougher, J. Bell, D. Brain, D. Mitchell, J. Luh-
707 mann, M. Holmström, H. Andersson, M. Yamauchi, A. Grigoriev, S. McKenna-Lawler,
708 J. R. Sharber, J. R. Scherrer, S. J. Jeffers, A. J. Coates, D. R. Linder, D. O. Kataria,
709 E. Kallio, H. Koskinen, T. Säles, P. Riihelä, W. Schmidt, E. Roelof, D. Williams,
710 S. Livi, C. C. Curtis, K. C. Hsieh, B. R. Sandel, M. Grande, M. Carter, J.-A. Sauvaud,
711 A. Fedorov, J.-J. Thocaven, S. Orsini, R. Cerulli-Irelli, M. Maggi, P. Wurz, P. Bochsler,
712 N. Krupp, J. Woch, M. Fränz, K. Asamura, and C. Dierker (2006), Numerical in-
713 terpretation of high-altitude photoelectron observations, *Icarus*, *182*, 383–395, doi:
714 10.1016/j.icarus.2005.10.036.

715 Lundin, R., S. Barabash, H. Andersson, M. Holmström, A. Grigoriev, M. Yamauchi, J.-A.
716 Sauvaud, A. Fedorov, E. Budnik, J.-J. Thocaven, D. Winningham, R. Frahm, J. Scherrer,
717 J. Sharber, K. Asamura, H. Hayakawa, A. Coates, D. R. Linder, C. Curtis, K. C. Hsieh,
718 B. R. Sandel, M. Grande, M. Carter, D. H. Reading, H. Koskinen, E. Kallio, P. Riihela,
719 W. Schmidt, T. Säles, J. Kozyra, N. Krupp, J. Woch, J. Luhmann, S. McKenna-Lawler,
720 R. Cerulli-Irelli, S. Orsini, M. Maggi, A. Mura, A. Milillo, E. Roelof, D. Williams,

721 S. Livi, P. Brandt, P. Wurz, and P. Bochsler (2004), Solar Wind-Induced Atmospheric
722 Erosion at Mars: First Results from ASPERA-3 on Mars Express, *Science*, 305(5692),
723 1933–1936, doi:10.1126/science.1101860.

724 Mantas, G. P., and W. B. Hanson (1979), Photoelectron fluxes in the Martian ionosphere,
725 *Journal of Geophysical Research*", 84, 369–385, doi:10.1029/JA084iA02p00369.

726 Matsunaga, K., K. Seki, D. A. Brain, T. Hara, K. Masunaga, J. P. McFadden, J. S.
727 Halekas, D. L. Mitchell, C. X. Mazelle, J. E. P. Connerney, and B. M. Jakosky (2015),
728 Comparison of Martian magnetic pileup boundary with ion composition boundary ob-
729 served by MAVEN, *AGU Fall Meeting Abstracts*.

730 Mitchell, D. L., R. P. Lin, H. Rème, D. H. Crider, P. A. Cloutier, J. E. P. Connerney,
731 M. H. Acuña, and N. F. Ness (2000), Oxygen auger electrons observed in Mars' iono-
732 sphere, *Geophysical Research Letters*", 27, 1871–1874, doi:10.1029/1999GL010754.

733 Mitchell, D. L., R. P. Lin, C. Mazelle, H. Rème, P. A. Cloutier, J. E. P. Connerney, M. H.
734 Acuña, and N. F. Ness (2001), Probing Mars' crustal magnetic field and ionosphere
735 with the MGS Electron Reflectometer, *Journal of Geophysical Research*", 106, 23,419–
736 23,428, doi:10.1029/2000JE001435.

737 Mitchell, D. L., C. Mazelle, J.-A. Sauvaud, J.-J. Thocaven, J. Rouzaud, A. Fedorov,
738 P. Rouger, D. Toublanc, E. Taylor, D. Gordon, M. Robinson, S. Heavner, P. Turin,
739 M. Diaz-Aguado, D. W. Curtis, R. P. Lin, and B. M. Jakosky (2016), The MAVEN
740 Solar Wind Electron Analyzer, *Space Science Reviews*", 200, 495–528, doi:
741 10.1007/s11214-015-0232-1.

742 Morschhauser, A., V. Lesur, and M. Grott (2014), A spherical harmonic model of the
743 lithospheric magnetic field of Mars, *Journal of Geophysical Research (Planets)*, 119,
744 1162–1188, doi:10.1002/2013JE004555.

745 Nagy, A. F., D. Winterhalter, K. Sauer, T. E. Cravens, S. Brecht, C. Mazelle, D. Crider,
746 E. Kallio, A. Zakharov, E. Dubinin, M. Verigin, G. Kotova, W. I. Axford, C. Bertucci,
747 and J. G. Trotignon (2004), The plasma Environment of Mars, *Space Science Reviews*,
748 111, 33–114, doi:10.1023/B:SPAC.0000032718.47512.92.

749 Ramstad, R., S. Barabash, Y. Futaana, H. Nilsson, X.-D. Wang, and M. Holmström
750 (2015), The Martian atmospheric ion escape rate dependence on solar wind and solar
751 EUV conditions: 1. Seven years of Mars Express observations, *Journal of Geophysical*
752 *Research (Planets)*, 120, 1298–1309, doi:10.1002/2015JE004816.

753 Riedler, W., K. Schwingenschuh, D. Moehlmann, V. N. Oraevskii, E. Eroshenko, and
754 J. Slavin (1989), Magnetic fields near Mars - First results, *Nature*, *341*, 604–607, doi:
755 10.1038/341604a0.

756 Rosenbauer, H., N. Shutte, A. Galeev, K. Gringauz, and I. Apathy (1989), Ions of Mar-
757 tian origin and plasma sheet in the Martian magnetosphere - Initial results of the TAUS
758 experiment, *Nature*, *341*, 612–614, doi:10.1038/341612a0.

759 Sakai, S., A. Rahmati, D. L. Mitchell, T. E. Cravens, S. W. Bougher, C. Mazelle, W. K.
760 Peterson, F. G. Eparvier, J. M. Fontenla, and B. M. Jakosky (2015), Model insights into
761 energetic photoelectrons measured at Mars by MAVEN, *Geophysical Research Letters*,
762 *42*, 8894–8900, doi:10.1002/2015GL065169.

763 Steckiewicz, M., C. Mazelle, P. Garnier, N. André, E. Penou, A. Beth, J.-A. Sauvaud,
764 D. Toubanc, D. L. Mitchell, J. P. McFadden, J. G. Luhmann, R. J. Lillis, J. E. P. Con-
765 nerney, J. R. Espley, L. Andersson, J. S. Halekas, D. E. Larson, and B. M. Jakosky
766 (2015), Altitude dependence of nightside Martian suprathermal electron depletions as
767 revealed by MAVEN observations, *Geophysical Research Letters*, *42*, 8877–8884, doi:
768 10.1002/2015GL065257.

769 Steckiewicz, M., P. Garnier, N. André, D. L. Mitchell, L. Andersson, E. Penou, A. Beth,
770 A. Fedorov, J.-A. Sauvaud, C. Mazelle, D. A. Brain, J. R. Espley, J. McFadden, J. S.
771 Halekas, D. E. Larson, R. J. Lillis, J. G. Luhmann, Y. Soobiah, and B. M. Jakosky
772 (2017), Comparative study of the Martian suprathermal electron depletions based on
773 Mars Global Surveyor, Mars Express, and Mars Atmosphere and Volatile Evolution
774 mission observations, *Journal of Geophysical Research (Space Physics)*, *122*, 857–873,
775 doi:10.1002/2016JA023205.

776 Trantham, M., M. Liemohn, D. Mitchell, and J. Frank (2011), Photoelectrons on closed
777 crustal field lines at Mars, *Journal of Geophysical Research (Space Physics)*, *116*,
778 A07311, doi:10.1029/2010JA016231.

779 Trotignon, J. G., C. Mazelle, C. Bertucci, and M. H. Acuña (2006), Martian shock and
780 magnetic pile-up boundary positions and shapes determined from the Phobos 2 and
781 Mars Global Surveyor data sets, *Planetary and Space Science*, *54*, 357–369, doi:
782 10.1016/j.pss.2006.01.003.

783 Tsang, S. M. E., A. J. Coates, G. H. Jones, R. A. Frahm, J. D. Winningham, S. Barabash,
784 R. Lundin, and A. Fedorov (2015), Ionospheric photoelectrons at Venus: Case stud-
785 ies and first observation in the tail, *Planetary and Space Science*, *113*, 385–394, doi:

786
787
788
789
790
791
792
793
794
795
796
797
798
799
800
801
802
803
804
805
806
807
808
809
810
811
812

10.1016/j.pss.2015.01.019.

Vignes, D., M. H. Acuna, J. E. P. Connerney, D. H. Crider, H. Reme, and C. Mazelle (2002), Factors controlling the location of the bow shock at mars, *Geophysical Research Letters*, 29(9), 42–1–42–4, doi:10.1029/2001GL014513.

Wellbrock, A., A. J. Coates, I. Sillanpää, G. H. Jones, C. S. Arridge, G. R. Lewis, D. T. Young, F. J. Crary, and A. D. Aylward (2012), Cassini observations of ionospheric photoelectrons at large distances from Titan: Implications for Titan’s exospheric environment and magnetic tail, *Journal of Geophysical Research (Space Physics)*, 117, A03216, doi:10.1029/2011JA017113.

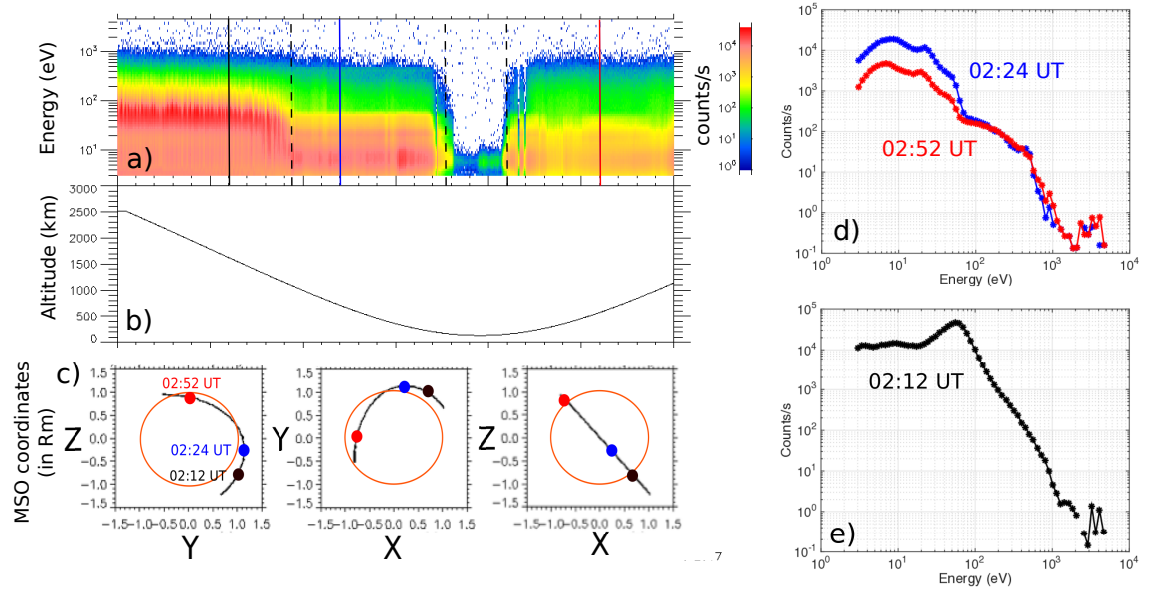
Xu, S., M. Liemohn, S. Bougher, and D. Mitchell (2015), Enhanced carbon dioxide causing the dust storm-related increase in high-altitude photoelectron fluxes at Mars, *Geophysical Research Letters*, 42, 9702–9710, doi:10.1002/2015GL066043.

Xu, S., D. Mitchell, M. Liemohn, C. Dong, S. Bougher, M. Fillingim, R. Lillis, J. McFadden, C. Mazelle, J. Connerney, and B. Jakosky (2016a), Deep nightside photoelectron observations by MAVEN SWEA: Implications for Martian northern hemispheric magnetic topology and nightside ionosphere source, *Geophysical Research Letters*, 43, 8876–8884, doi:10.1002/2016GL070527.

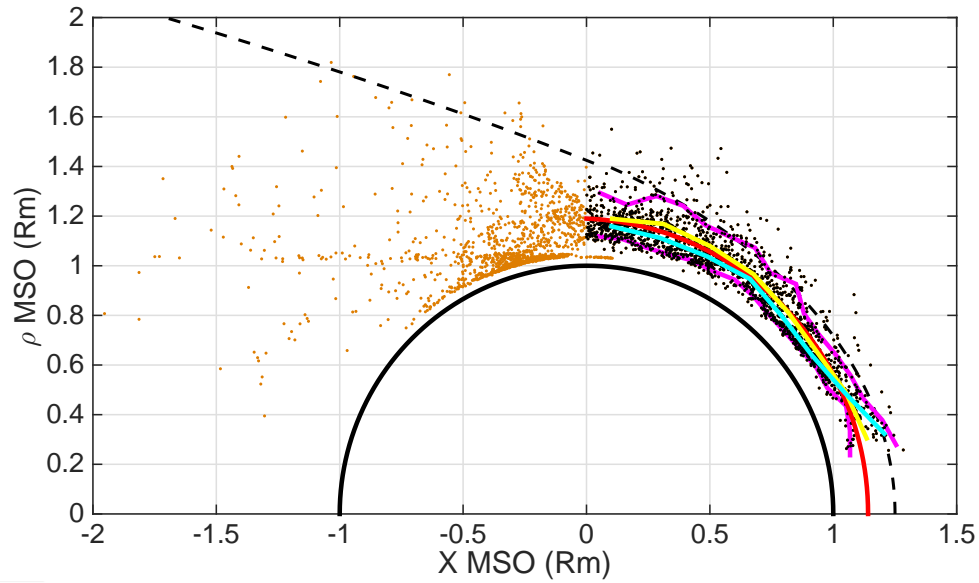
Xu, S., M. Liemohn, S. Bougher, and D. Mitchell (2016b), Martian high-altitude photoelectrons independent of solar zenith angle, *Journal of Geophysical Research (Space Physics)*, 121, 3767–3780, doi:10.1002/2015JA022149.

Xu, S., M. W. Liemohn, C. Dong, D. L. Mitchell, S. W. Bougher, and Y. Ma (2016c), Pressure and ion composition boundaries at Mars, *Journal of Geophysical Research (Space Physics)*, 121, 6417–6429, doi:10.1002/2016JA022644.

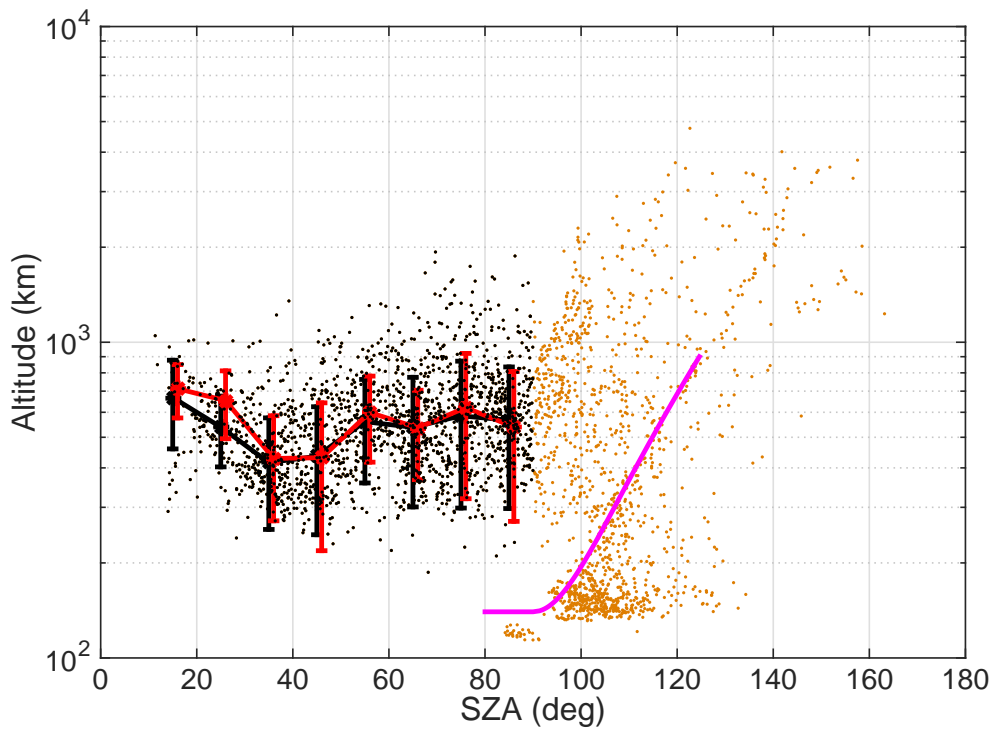
Xu, S., D. Mitchell, M. Liemohn, X. Fang, Y. Ma, J. Luhmann, D. Brain, M. Steckiewicz, C. Mazelle, J. Connerney, and B. Jakosky (2017), Martian low-altitude magnetic topology deduced from MAVEN/SWEA observations, *Journal of Geophysical Research: Space Physics*, 122(2), 1831–1852, doi:10.1002/2016JA023467, 2016JA023467.



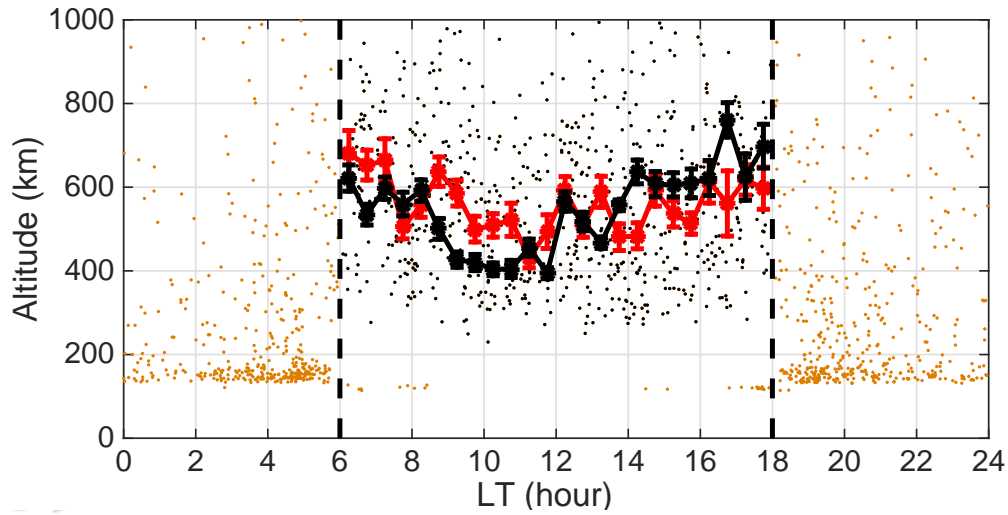
813 **Figure 1.** Case study on February 12 2015. Panel a: MAVEN SWEA electron energy spectrogram with the
 814 colorbar giving the omnidirectional counts/s. The dashed black lines show the crossings of the 20 – 30 eV
 815 photoelectron line, while the black/blue/red solid lines correspond to the times of the individual energy spec-
 816 tra given in panels d and e. Panel b: altitude of the spacecraft. Panel c: (X,Y,Z) coordinates of the spacecraft
 817 in the MSO frame, where X points towards the Sun, Y points opposite to Mars orbital angular velocity and
 818 Z completes the right-handed set. Panel d: SWEA electron energy spectra typical for the dense ionosphere
 819 (blue) or escaping photoelectrons (red) in the tail. Panel e: typical magnetosheath SWEA electron spectrum.



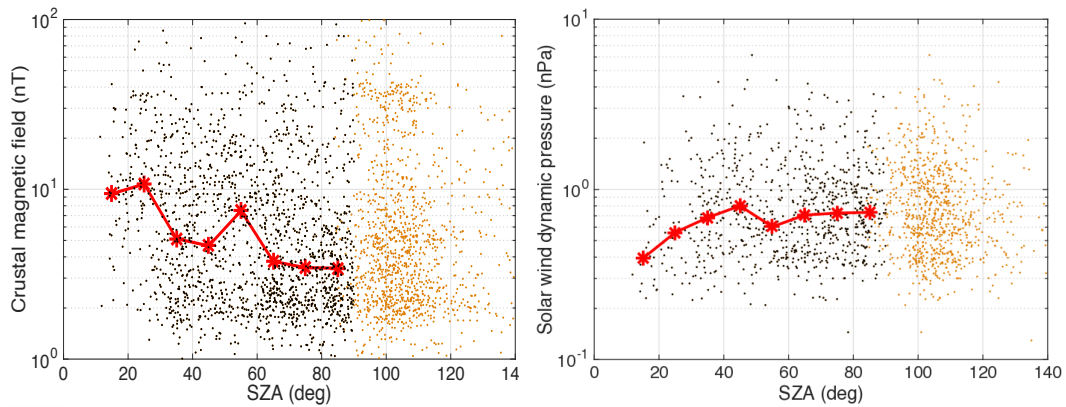
820 **Figure 2.** Geographical distribution of the photoelectron line crossings - PEB crossings in black dots, other
 821 crossings in orange - in cylindrical coordinates (in the plane (X, ρ) with $\rho = \sqrt{Y^2 + Z^2}$ the distance to the X
 822 axis ; $1R_M \approx 3390 \text{ km}$ average Martian radius). The dashed black line provides the average location of the
 823 Magnetic Pile-Up Boundary fit by *Trotignon et al.* [2006]. The cyan and yellow solid lines show respectively
 824 the northern and southern median location of the PEB (for 10° solar zenith angle bins), while the red curve
 825 shows the best conic fit for the dayside PEB crossings (see text for more details). The magenta lines show the
 826 limits including 80% of the PEB crossings.



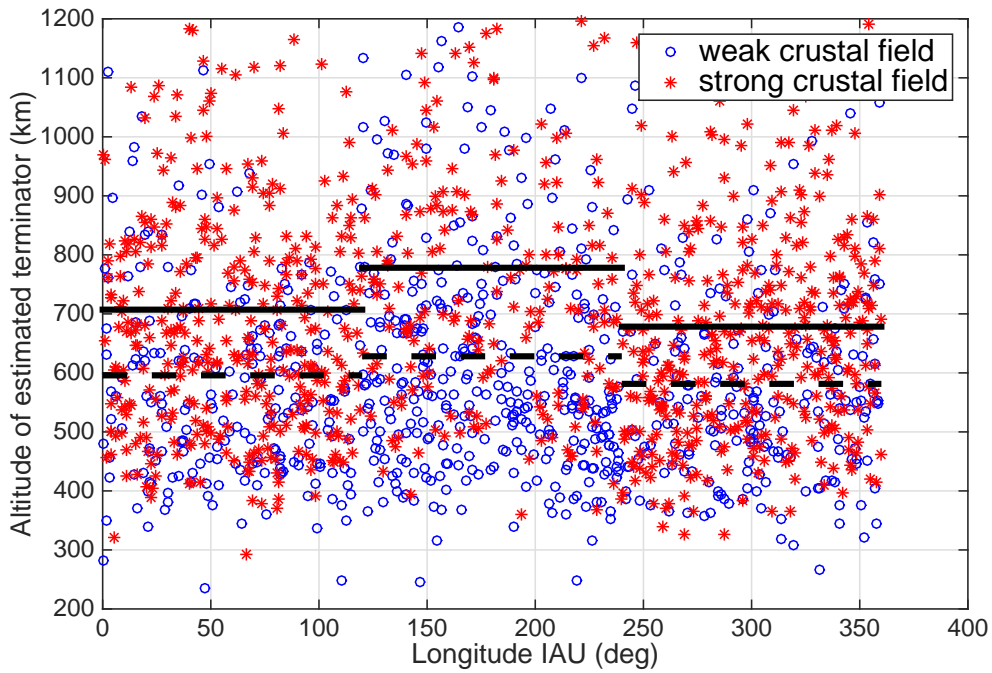
827 **Figure 3.** Altitude of the photoelectron line crossings - PEB crossings in black dots, other crossings in
 828 orange - as a function of the solar zenith angle (SZA). The magenta solid line provides the extreme ultraviolet
 829 terminator limit (where most photons are absorbed) corresponding to a lower limit at 140 km altitude. The
 830 black solid line shows the median altitude for SZA bins of 20° with the standard deviation, while the red solid
 831 line shows the median and standard deviation altitude for SZA values recalculated after including the aberration
 832 angle induced by the solar wind and after rotating the initial MSO frame into the MSE frame (see text for
 833 further details).



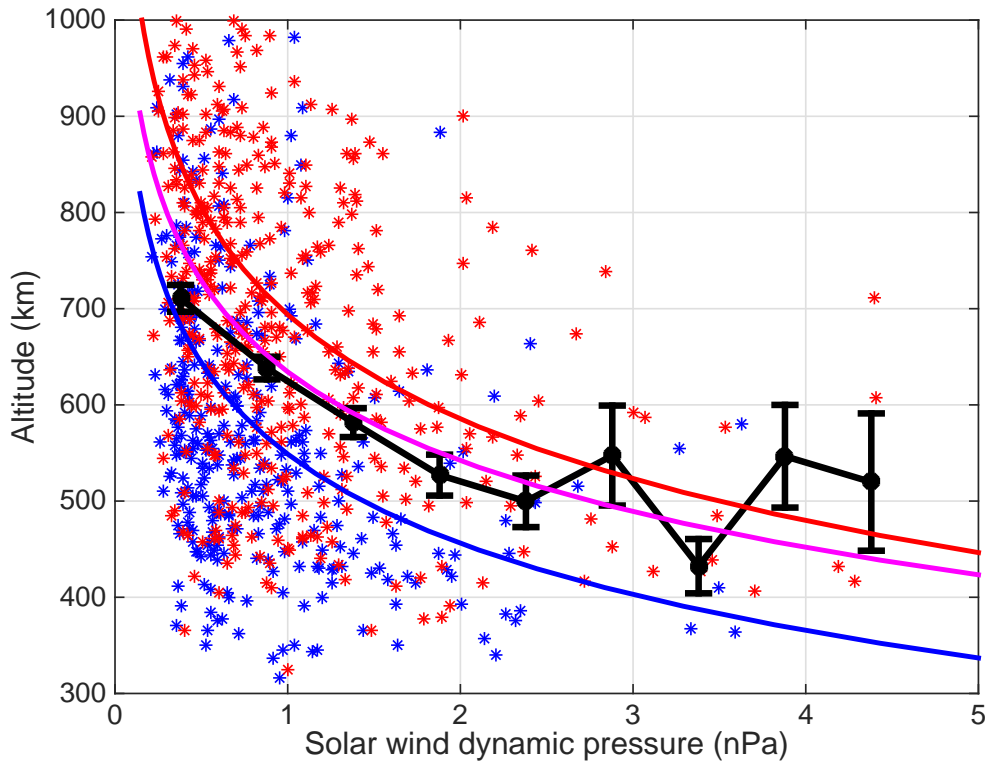
834 **Figure 4.** Altitude of the photoelectron line crossings - PEB crossings in black dots, other crossings in
 835 orange - as a function of the local time (LT). The dashed lines show the terminator while the solid lines show
 836 the median altitude for LT bins of 0.5 hour in the initial MSO frame (black line) and in the MSE frame (red
 837 line) that also includes the aberration angle induced by the solar wind (see text for further details).



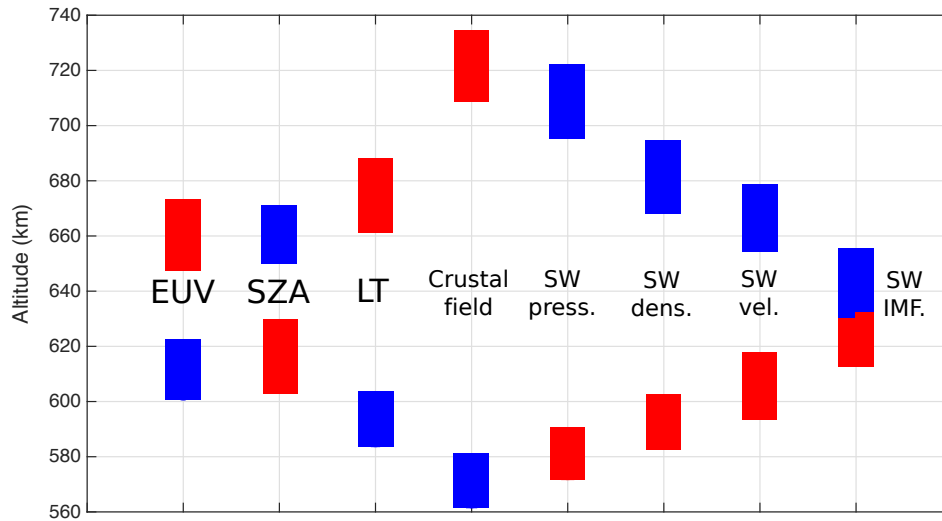
838 **Figure 5.** Demonstration of the SZA sampling bias for the PEB crossings dataset : SZA variability of the
 839 crustal magnetic field (left panel) and solar wind dynamic pressure (right panel) at the times of the photoelec-
 840 tron line crossings, with PEB crossings in black dots, other crossings in orange and the median values as solid
 841 red line. The crustal magnetic field is given by the *Morschauer et al.* [2014] model at a constant altitude of
 842 400 km.



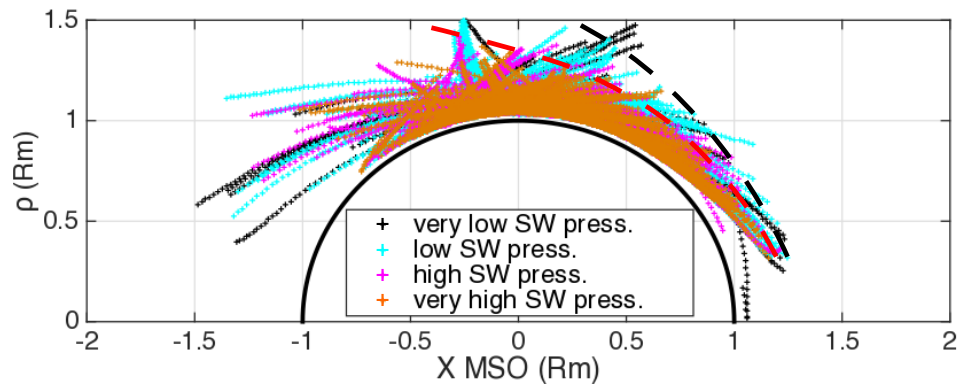
843 **Figure 6.** Estimated terminator altitude of the PEB crossings as a function of the longitude in the geograph-
 844 ical IAU frame. The dataset is separated into longitude and latitude regions to separate the strong and weak
 845 crustal field regimes, as defined by *Edberg et al.* [2008] (see text for more details). The blue circles and red
 846 stars correspond to PEB crossings in weak and strong crustal field regions, while the solid and dashed lines
 847 correspond to median altitudes for respectively strong and weak crustal field conditions in each of the three
 848 longitude bins.



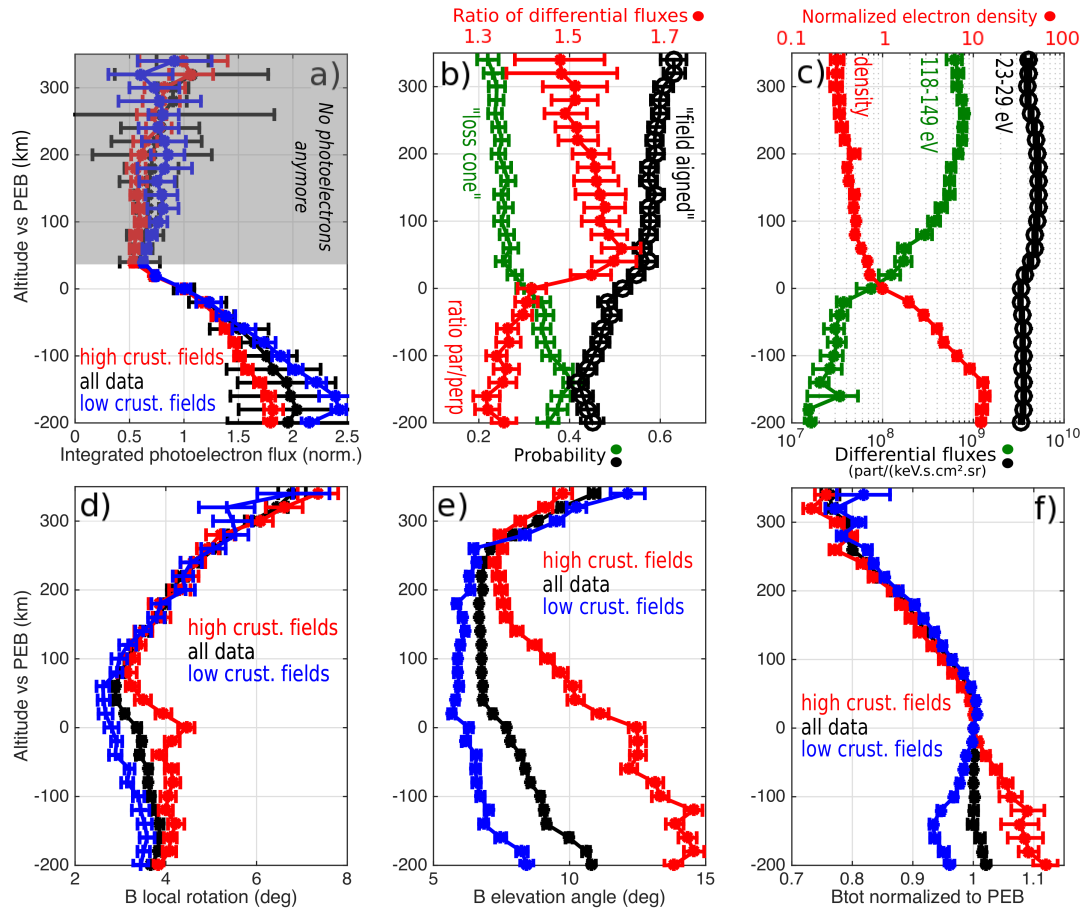
849 **Figure 7.** Estimated terminator altitude of the PEB crossings as a function of the solar wind dynamic pres-
 850 sure. The blue and red stars correspond respectively to weak and strong crustal field regions (based on the
 851 same definition as in figure 6). The solid black line provides the median altitude (and standard deviation of the
 852 median) for 0.5 nPa bins. The magenta / blue / red solid lines give the best power law fits (see section 3.2 for
 853 further details) of all / weak crustal field / strong crustal field crossings.



854 **Figure 8.** Compared influence of a number of parameters on the PEB terminator altitude: extreme ul-
855 traviolet (EUV) fluxes, solar zenith angle (SZA), local time (LT), crustal magnetic field, solar wind (SW)
856 dynamic pressure (press.), density, (dens.) velocity (vel.) and magnetic field (IMF). Each set of parameters
857 was separated into low (below the median value of the parameter) and high (above the median value of the
858 parameter) subsets of data. The median and standard deviation of the median are then calculated for the low
859 and high subsets of each parameter, shown by rectangles in the figure (blue/red for the low/high subsets, with
860 the height giving twice the standard deviation of the median). The rectangles of low/high subsets of the solar
861 wind IMF cross each other, since the standard deviations overlap. The EUV fluxes are derived from the FISM
862 model (*Chamberlin et al. [2007]* ; available on the CDP/AMDA database) at the 30.4 nm solar spectrum line
863 which is the source of the 20 – 30 eV photoelectrons ; the crustal magnetic field pressure is calculated from
864 the *Morschhauser et al. [2014]* model at a constant altitude of 400 km ; the solar wind parameters are derived
865 from the MAVEN SWIA and MAG data [*Halekas et al., 2017*].

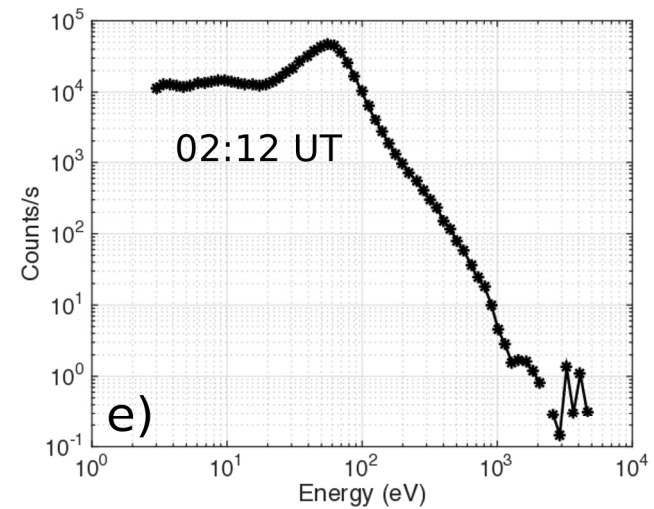
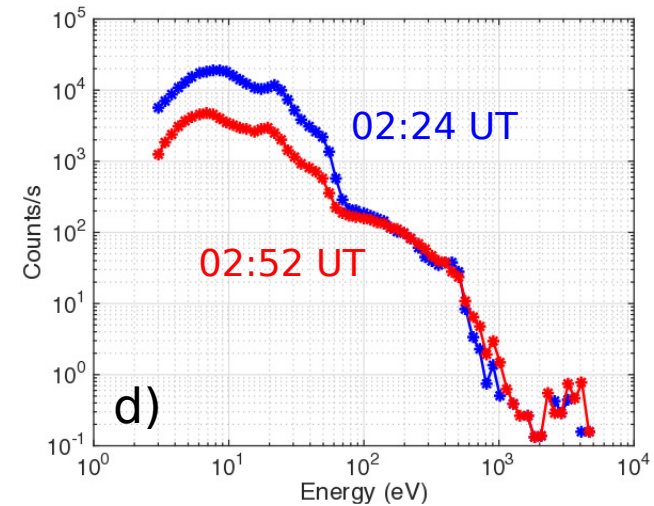
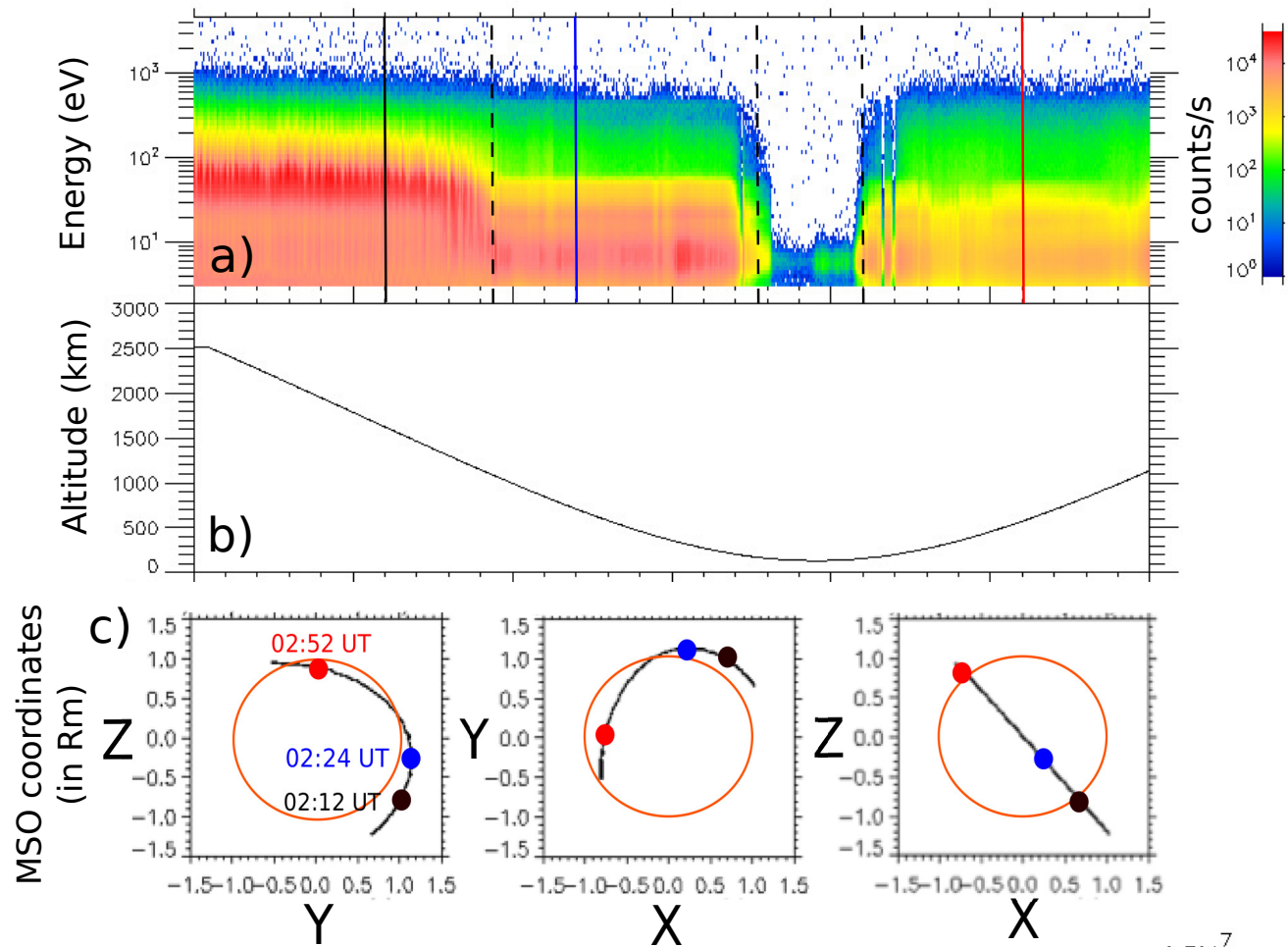


866 **Figure 9.** Influence of the solar wind dynamic pressure on the 20 – 30 eV photoelectron detection location
 867 in cylindrical MSO coordinates, assuming a continuous detection between inbound and outbound photo-
 868 electron line crossings and four levels of solar wind dynamic pressure conditions: very low corresponds to
 869 the $P_{SW} \leq 25\%$ quantile, low to $25\% < P_{SW} \leq 50\%$, high to $50\% < P_{SW} \leq 75\%$, very high
 870 to $P_{SW} > 75\%$. The two dashed lines represent sketched minimum and maximum altitude shapes for the
 871 photoelectron transport (see section 4 for more details).

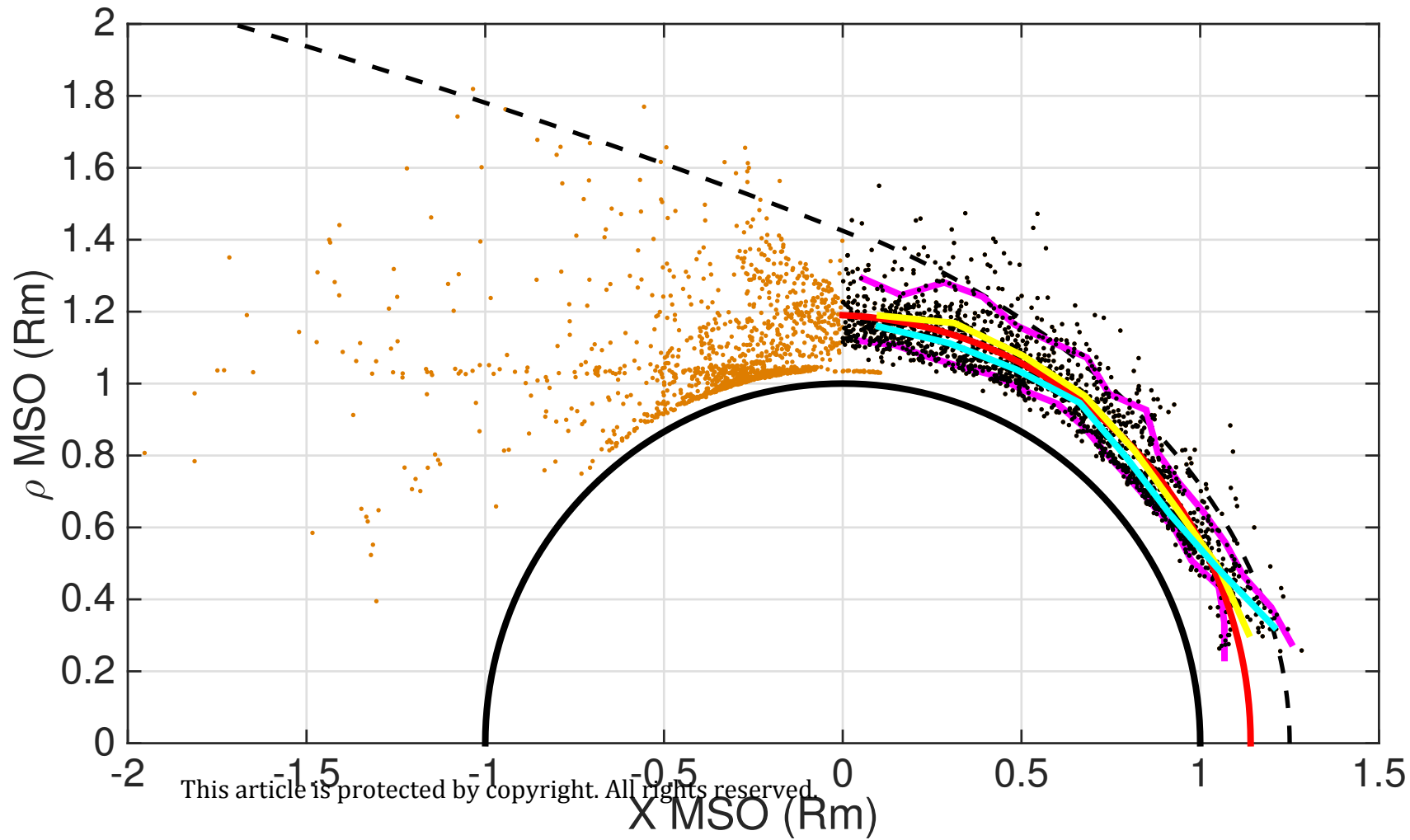


872 **Figure 10.** Average evolution of various parameters (eventually normalized, by the value at the PEB) as
 873 a function of altitude versus the PEB altitude (0 means the PEB altitude). Panel a): normalized integrated
 874 20 – 30 eV photoelectron flux from SWEA (shadowed part indicates incorrect photoelectron flux values);
 875 black / blue / red lines (as for panels d) e) f)) respectively correspond to all PEB crossings / only low crustal
 876 fields crossings / only high crustal fields crossings (see text). Panel b): pitch angle information on 23 – 29 eV
 877 electrons: maximum ratio between parallel and perpendicular differential fluxes, probability of "loss cone" or
 878 "field aligned" pitch angle distributions for the 0 – 90° range. Panel (c): mean SWEA differential fluxes of
 879 23 – 29 eV and 118 – 149 eV electrons, and thermal electron density by LPW. Panels d) e) f): local angular
 880 rotation / elevation angle / normalized total magnitude of the in situ magnetic field measured by MAG. See
 881 text for more details.

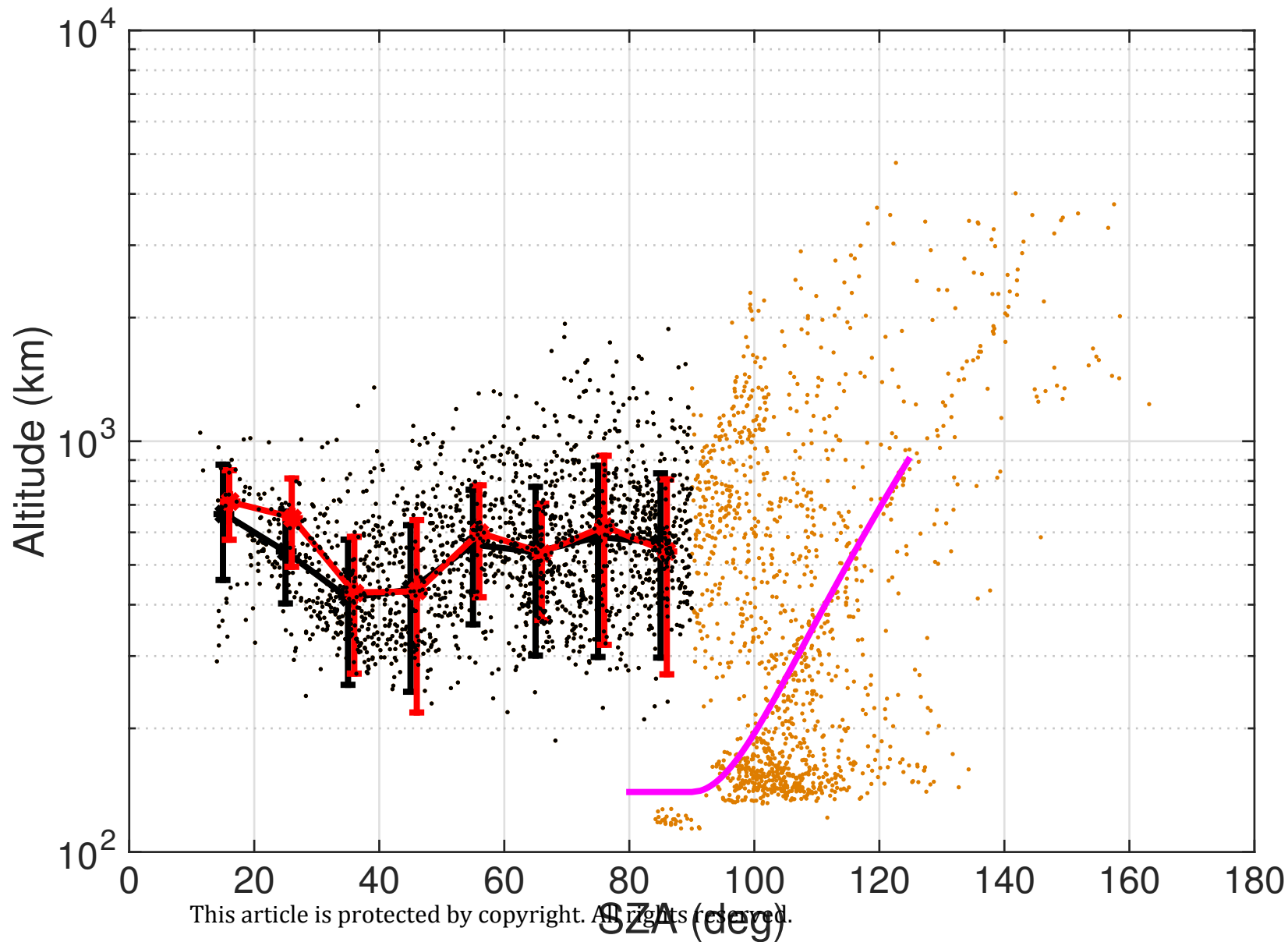
Author Manuscript



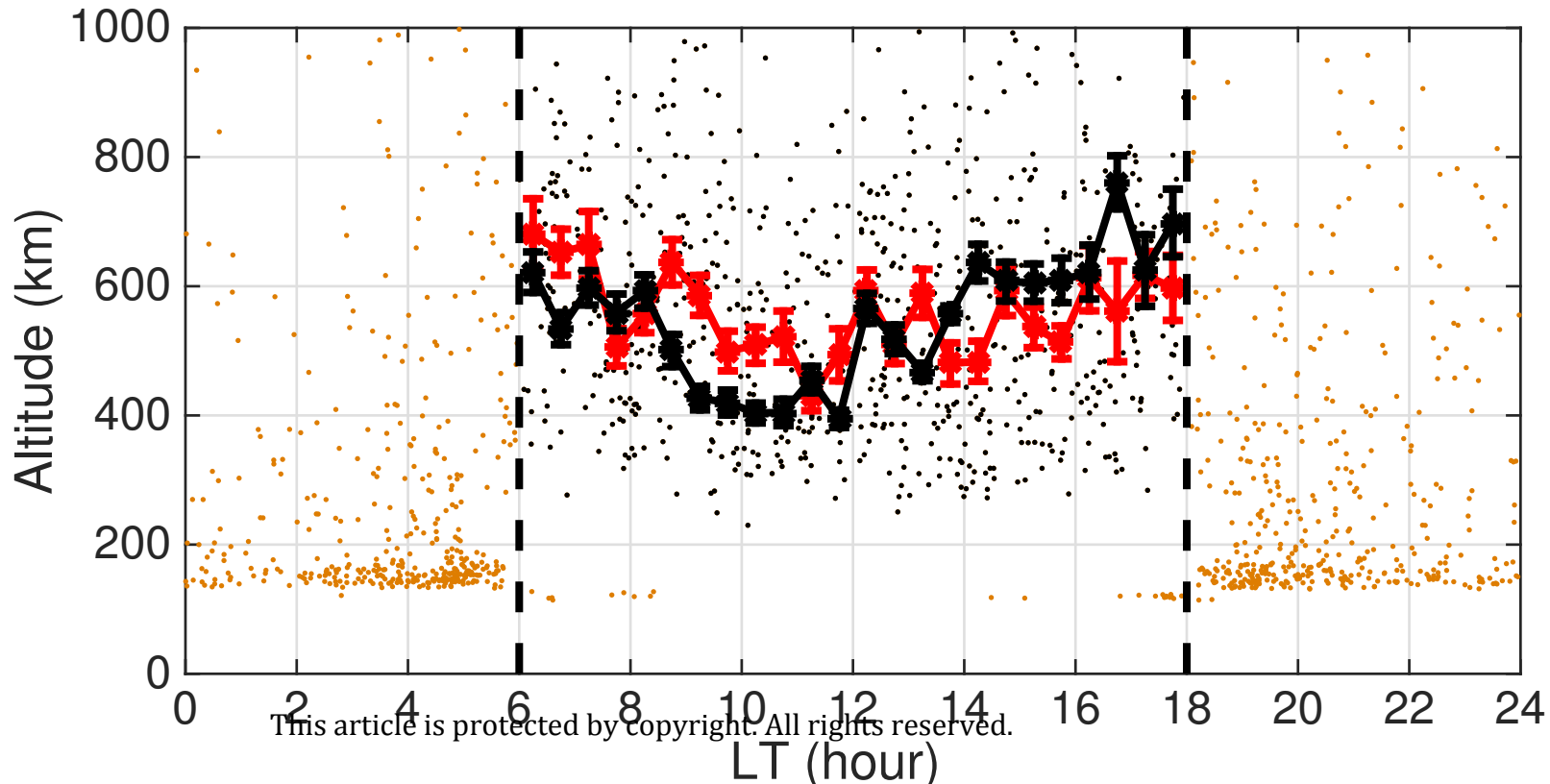
Author Manuscript



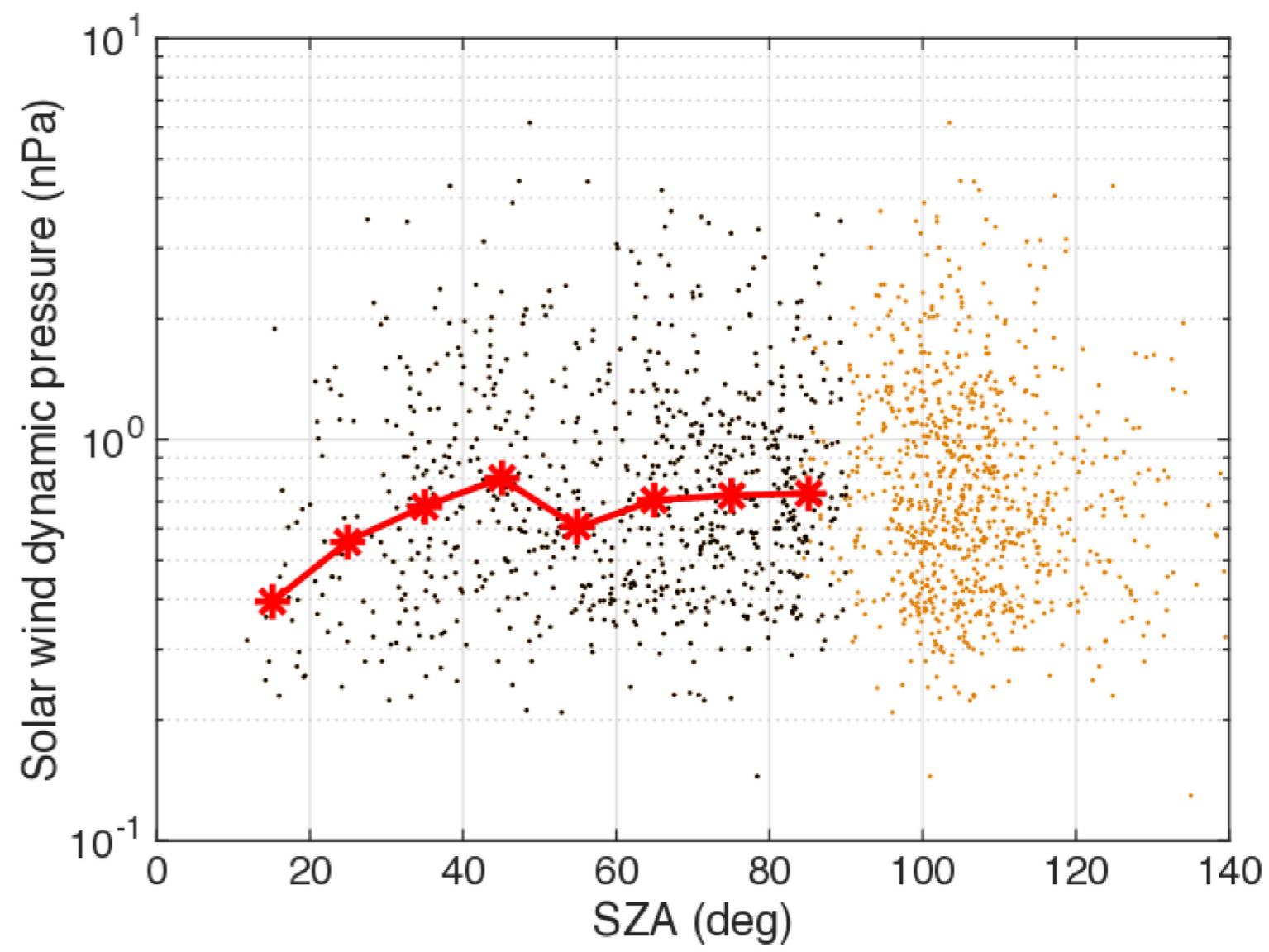
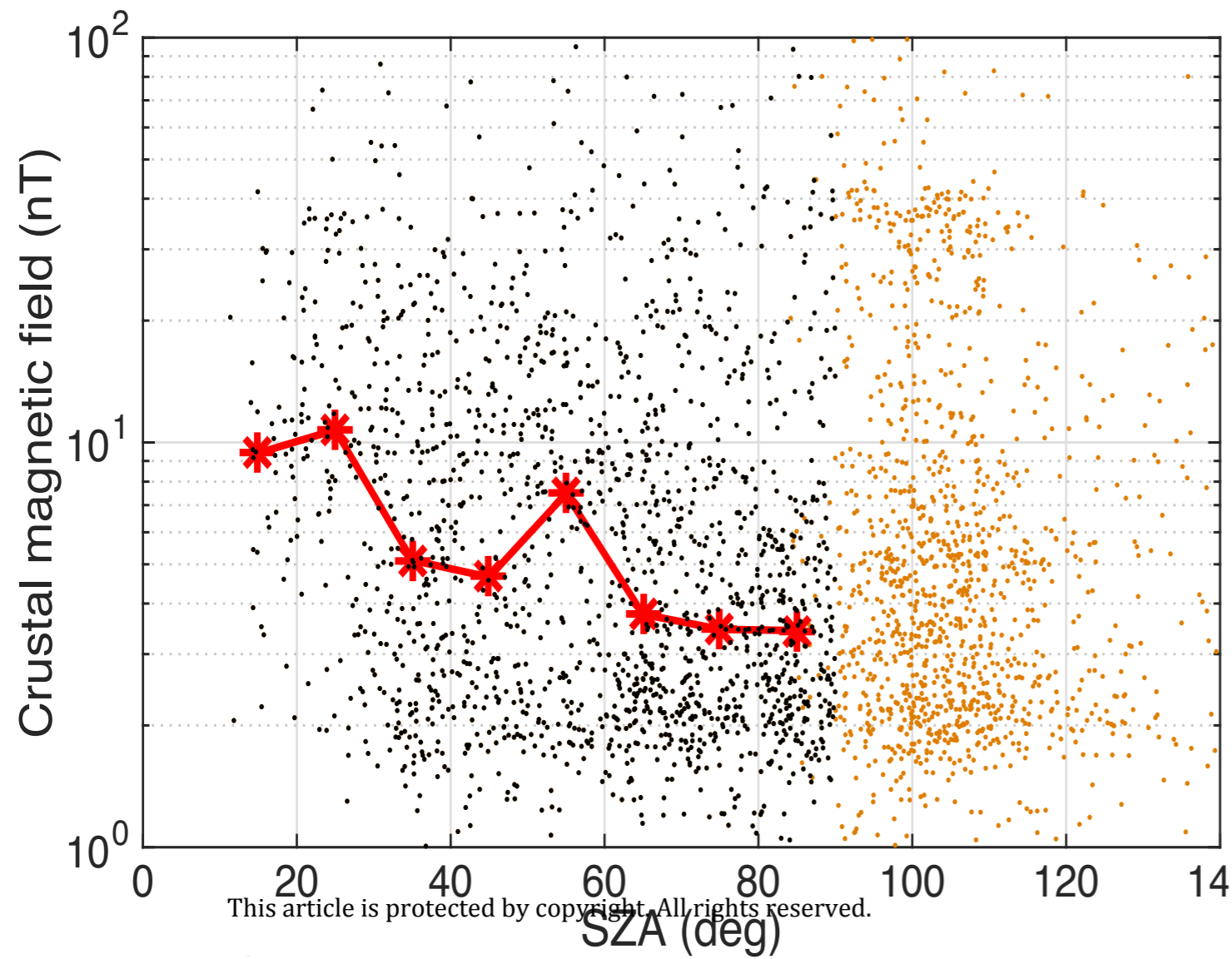
Author Manuscript



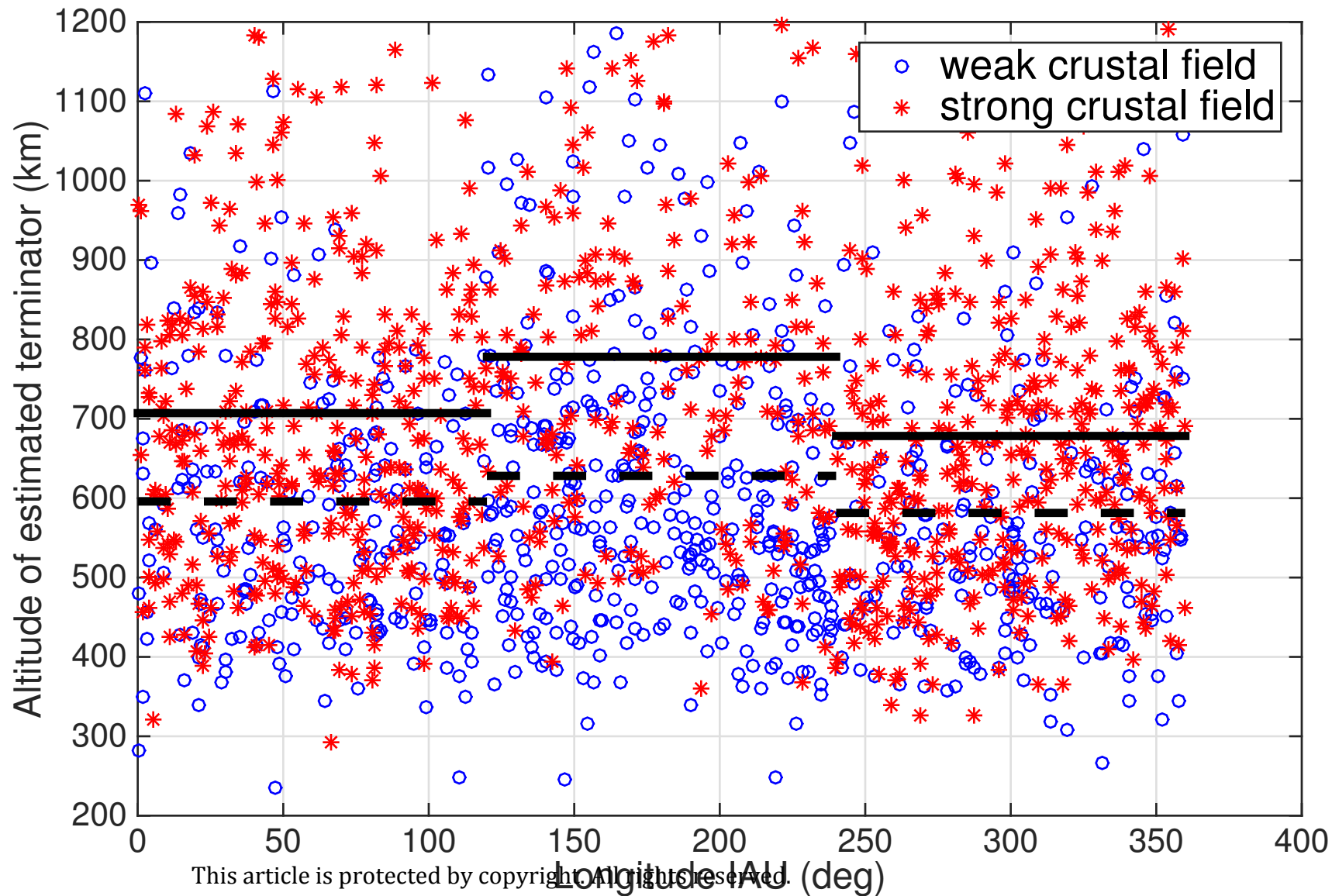
Author Manuscript



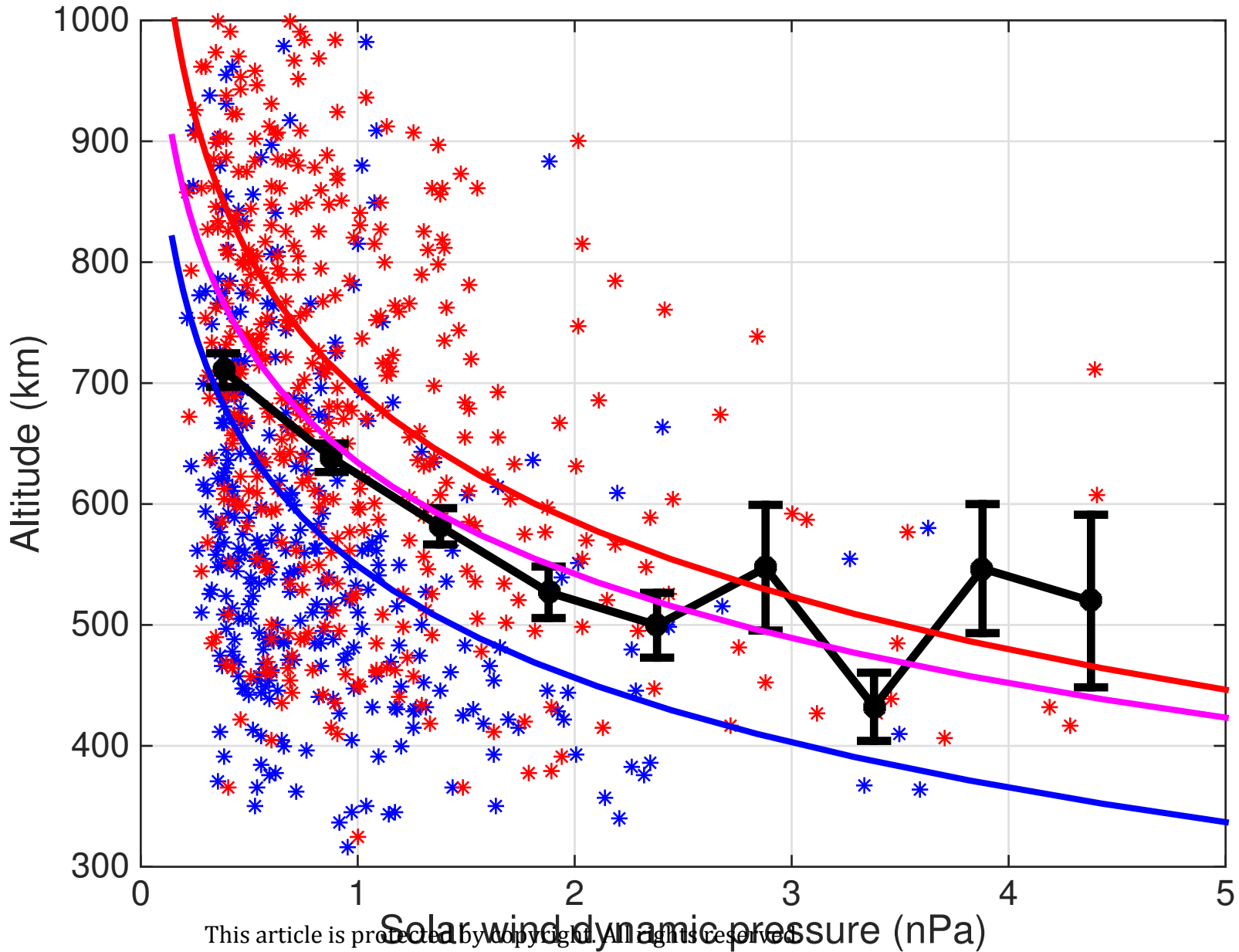
Author Manuscript



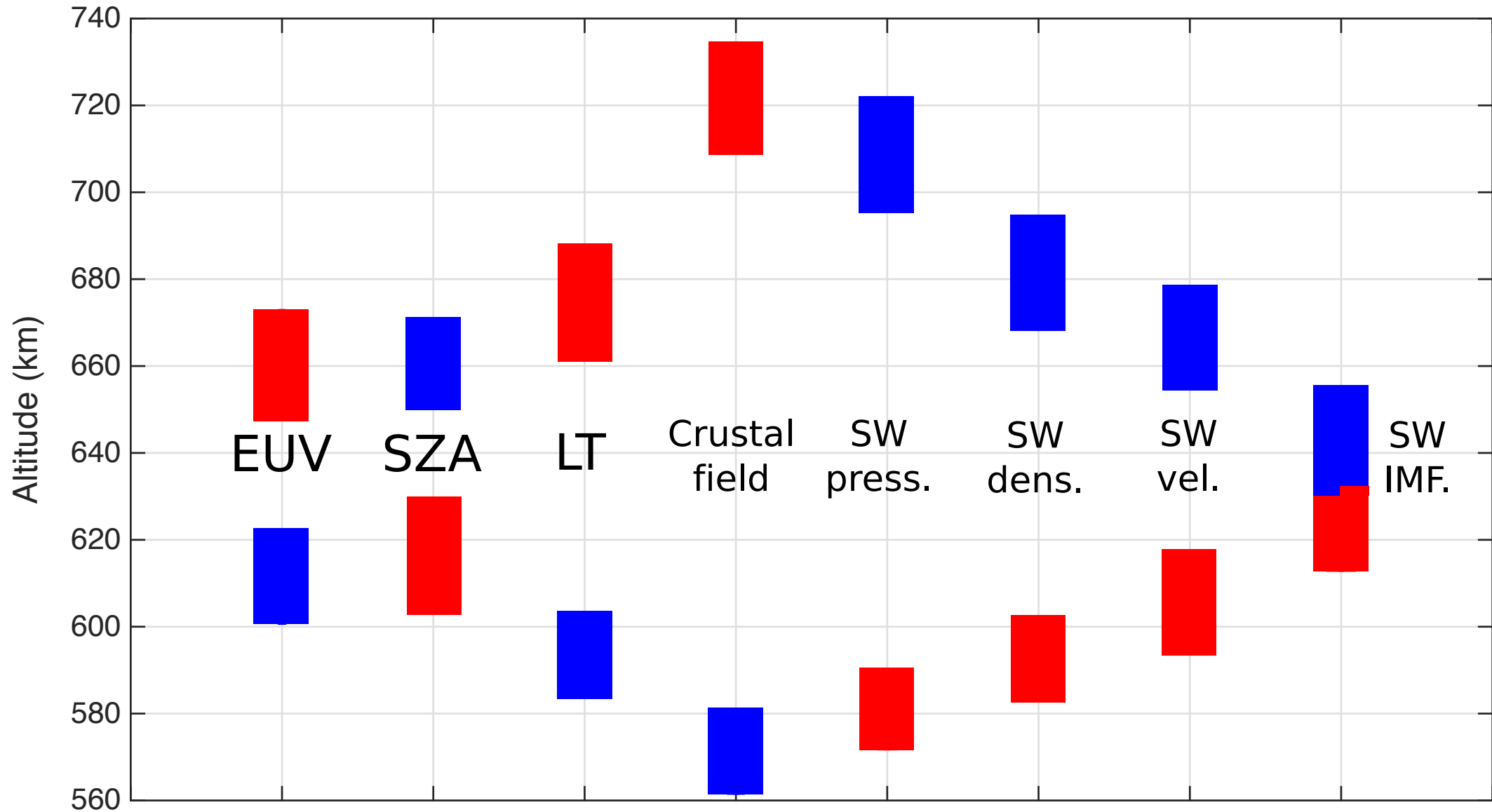
Author Manuscript



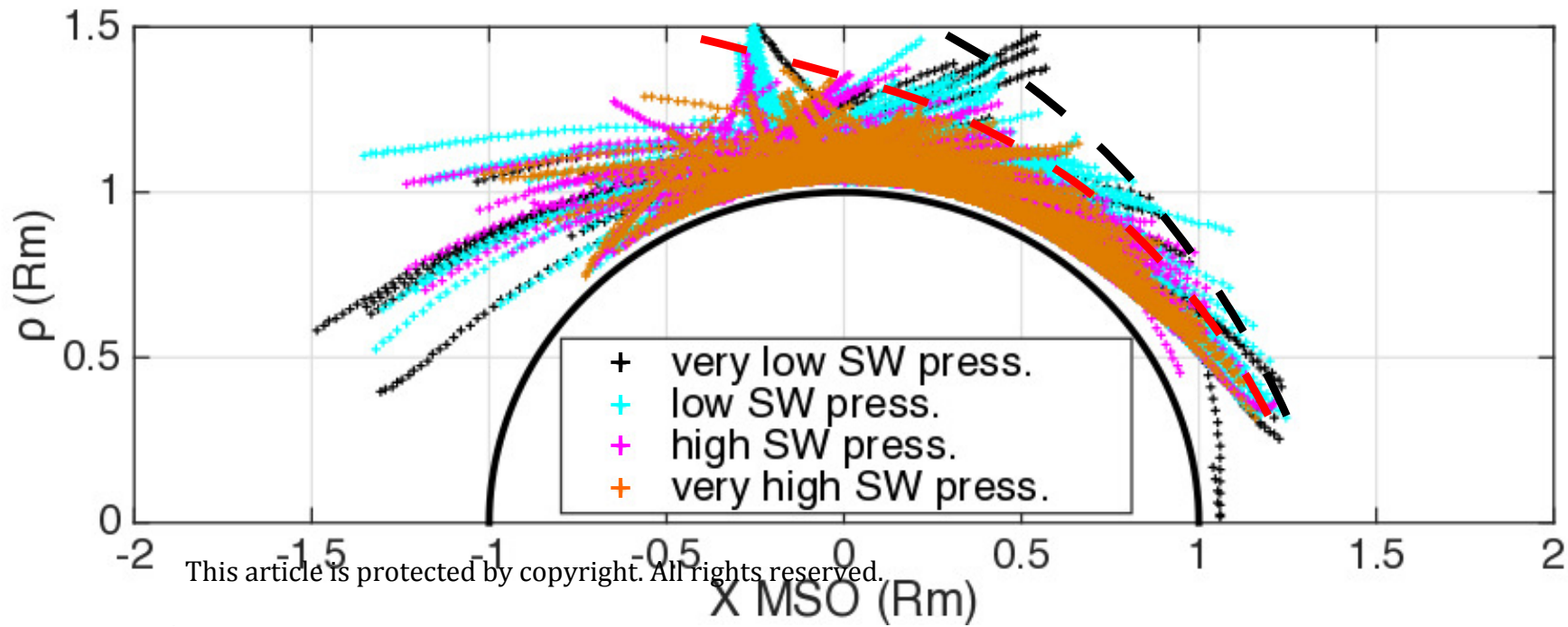
Author Manuscript



Author Manuscript



Author Manuscript



Author Manuscript

